



HAL
open science

Expanding bubbles in Orion A: [C II] observations of M 42, M 43, and NGC 1977

C. H. M. Pabst, J. R. Goicoechea, D. Teyssier, O. Berné, R. D. Higgins, E. T. Chambers, S. Kabanovic, R. Güsten, J. Stutzki, A. G. G. M. Tielens

► To cite this version:

C. H. M. Pabst, J. R. Goicoechea, D. Teyssier, O. Berné, R. D. Higgins, et al.. Expanding bubbles in Orion A: [C II] observations of M 42, M 43, and NGC 1977. *Astronomy and Astrophysics - A&A*, 2020, 639, 10.1051/0004-6361/202037560 . insu-03673141

HAL Id: insu-03673141

<https://insu.hal.science/insu-03673141>

Submitted on 20 May 2022

HAL is a multi-disciplinary open access archive for the deposit and dissemination of scientific research documents, whether they are published or not. The documents may come from teaching and research institutions in France or abroad, or from public or private research centers.

L'archive ouverte pluridisciplinaire **HAL**, est destinée au dépôt et à la diffusion de documents scientifiques de niveau recherche, publiés ou non, émanant des établissements d'enseignement et de recherche français ou étrangers, des laboratoires publics ou privés.

Expanding bubbles in Orion A: [C II] observations of M 42, M 43, and NGC 1977

C. H. M. Pabst¹, J. R. Goicoechea², D. Teyssier³, O. Berné⁴, R. D. Higgins⁵, E. T. Chambers⁷, S. Kabanovic⁵, R. Güsten⁶, J. Stutzki⁵, and A. G. G. M. Tielens¹

¹ Leiden Observatory, Leiden University, PO Box 9513, 2300 RA Leiden, The Netherlands
e-mail: pabst@strw.leidenuniv.nl

² Instituto de Física Fundamental, CSIC, Calle Serrano 121-123, 28006 Madrid, Spain

³ Telespazio Vega UK Ltd. for ESA/ESAC, Urbanizacion Villafranca del Castillo, 28691 Madrid, Spain

⁴ IRAP, Université de Toulouse, CNRS, CNES, UPS, 9 Av. colonel Roche, 31028 Toulouse Cedex 4, France

⁵ I. Physikalisches Institut der Universität zu Köln, Zùlpicher Strasse 77, 50937 Köln, Germany

⁶ Max-Planck-Institut für Radioastronomie, Auf dem Hügel 69, 53121 Bonn, Germany

⁷ USRA/SOFIA, NASA Ames Research Center, Mail Stop 232-12, Building N232, PO Box 1, Moffett Field, CA 94035-0001, USA

Received 23 January 2020 / Accepted 22 April 2020

ABSTRACT

Context. The Orion Molecular Cloud is the nearest massive-star forming region. Massive stars have profound effects on their environment due to their strong radiation fields and stellar winds. Stellar feedback is one of the most crucial cosmological parameters that determine the properties and evolution of the interstellar medium in galaxies.

Aims. We aim to understand the role that feedback by stellar winds and radiation play in the evolution of the interstellar medium. Velocity-resolved observations of the [C II] 158 μm fine-structure line allow us to study the kinematics of UV-illuminated gas. Here, we present a square-degree-sized map of [C II] emission from the Orion Nebula complex at a spatial resolution of 16'' and high spectral resolution of 0.2 km s⁻¹, covering the entire Orion Nebula (M 42) plus M 43 and the nebulae NGC 1973, 1975, and 1977 to the north. We compare the stellar characteristics of these three regions with the kinematics of the expanding bubbles surrounding them.

Methods. We use [C II] 158 μm line observations over an area of 1.2 deg² in the Orion Nebula complex obtained by the upGREAT instrument onboard SOFIA.

Results. The bubble blown by the O7V star θ^1 Ori C in the Orion Nebula expands rapidly, at 13 km s⁻¹. Simple analytical models reproduce the characteristics of the hot interior gas and the neutral shell of this wind-blown bubble and give us an estimate of the expansion time of 0.2 Myr. M 43 with the B0.5V star NU Ori also exhibits an expanding bubble structure, with an expansion velocity of 6 km s⁻¹. Comparison with analytical models for the pressure-driven expansion of H II regions gives an age estimate of 0.02 Myr. The bubble surrounding NGC 1973, 1975, and 1977 with the central B1V star 42 Orionis expands at 1.5 km s⁻¹, likely due to the over-pressurized ionized gas as in the case of M 43. We derive an age of 0.4 Myr for this structure.

Conclusions. We conclude that the bubble of the Orion Nebula is driven by the mechanical energy input by the strong stellar wind from θ^1 Ori C, while the bubbles associated with M 43 and NGC 1977 are caused by the thermal expansion of the gas ionized by their central later-type massive stars.

Key words. ISM: bubbles – ISM: kinematics and dynamics – infrared: ISM

1. Introduction

Stellar feedback, that is injection of energy and momentum from stars, is one of the most important input parameters in cosmological models that simulate and explain the evolution of our universe. Even small variations in this crucial parameter can lead to drastic changes in the results. Too much stellar feedback of early stars disrupts the ambient gas in too early a stage to form more stars and, eventually, planetary systems that allow for the formation of life. Too little feedback fails to prevent the interstellar gas from gravitational collapse to dense, cold clumps. Stellar feedback is often quantified as the star-formation rate (SFR), the rate at which (mostly low-mass) stars are formed. Studies on the interaction of massive stars with their environment generally focus on the effects of supernova explosions injecting mechanical energy into their environment and the radiative interaction leading to the ionization and thermal expansion of the gas. The

explosion of a massive star ejects some 10 M_{\odot} at velocities of some 10 000 km s⁻¹, injecting about 10⁵¹ erg into the surrounding medium. The hot plasma created by the reverse shock drives the expansion of the supernova remnant. The concerted effects of many supernovae in an OB association create superbubbles that expand perpendicular to the plane and may break open, releasing the hot plasma and any entrained colder cloud material into the lower halo (McKee & Ostriker 1977; McCray & Kafatos 1987; Mac Low & McCray 1988; Norman & Ikeuchi 1989; Hopkins et al. 2012).

However, there is evidence that also stellar winds have a profound impact on the interstellar medium (ISM). Observations and models have long attested to the importance of stellar winds from massive stars as sources of mechanical energy that can have profound influence on the direct environment (Castor et al. 1975; Weaver et al. 1977; Wareing et al. 2018; Pabst et al. 2019). These stellar winds drive a strong shock into its surroundings, which

sweeps up ambient gas into dense shells. At the same time, the reverse shock stops the stellar wind, creating a hot tenuous plasma. Eventually, the swept up shells break open, venting their hot plasma into the surrounding medium.

Feedback by ionization of the gas surrounding a massive star will also lead to the disruption of molecular clouds (Williams & McKee 1997; Freyer et al. 2006; Dale et al. 2013). Initially, this will be through the more or less spherical expansion driven by the high pressure of the H II region (Spitzer 1978). Once this expanding bubble breaks open into the surrounding low density material, a champagne flow will be set up (Bedijn & Tenorio-Tagle 1981), rapidly removing material from the molecular cloud.

Bubble structures are ubiquitous in the ISM (e.g., Churchwell et al. 2006). Most of these are caused by expanding H II regions (Walch et al. 2013; Ochsendorf et al. 2014). However, due to the clumpy structure of the ISM, and molecular clouds in particular, the expanding shock fronts can be highly irregular. Depending on the morphology of the shock front, that is the formation of a shell and more or less massive clumps, massive star formation can be either triggered or hindered (e.g., Walch et al. 2012).

The relative importance of these three different feedback processes (SNe, stellar winds, thermal expanding H II regions) is controversial. Given the peculiar motion of massive stars, SN explosions may occur at relatively large distances from their natal clouds and therefore have little effect on the cloud as the energy is expended in rejuvenating plasma from previous SN explosions, sweeping up tenuous intercloud material and transporting it to the superbubble walls (McKee & Ostriker 1977; Mac Low & McCray 1988; Norman & Ikeuchi 1989; Ochsendorf et al. 2015). While the mechanical energy output in terms of stellar winds is much less than from SN explosions, they will act directly on the natal cloud.

The Orion molecular cloud is the nearest region of massive star formation and has been studied in a wide range of wavelengths. The dense molecular cloud is arranged in an integral-shaped filament (ISF), which has fragmented into four cores, OMC1, 2, 3, and 4, that are all active sites of star formation. At the front side of the most massive core, OMC1, the massive O7V star θ^1 Ori C has ionized the well-known H II region M42 (NGC 1976), that is known as the Orion Nebula. The Orion Nebula, appearing as the middle “star” in the sword of Orion at a distance of $d \approx 414$ pc from us (Menten et al. 2007), is one of the most picturesque structures of our universe. The strong stellar wind from this star has created a bubble filled with hot plasma that is rapidly expanding into the lower-density gas located at the front of the core (Güdel et al. 2008; Pabst et al. 2019). In addition, two slightly less massive stars, B0.5V-type NU Ori and B1V-type 42 Orionis, have created their own ionized gas bubbles, M43 and NGC 1977. These stars are not expected to have strong stellar winds and likely the thermal pressure of the ionized gas dominates the expansion of these two regions.

The current picture is as follows¹: the Trapezium cluster including θ^1 Ori C, the most massive stars in the Orion Nebula complex, is situated at the surface of its natal molecular cloud, the OMC1 region of the Orion A molecular cloud. Presumably, the Trapezium stars live in a valley of the molecular cloud, having swept away the covering cloud layers (see O’Dell et al.

2009 for a detailed discussion of the structure of the inner Orion Nebula). In the immediate environment of the Trapezium stars, the gas is warm and ionized, constituting a dense H II region, the Huygens Region. It is confined towards the back by the dense molecular cloud core and this is exemplified by the prominent ionization front to the south, the Orion Bar, a narrow and very dense structure Tielens et al. (1993); Goicoechea et al. (2016). To the west of the Trapezium stars, embedded in the molecular gas of OMC1, one finds two dense cores with violent emission features, strong outflows and shocked molecular gas, that are the sites of active intermediate- and high-mass star formation, the Becklin-Neugebauer/Kleinmann-Low (BN/KL) region and Orion South (S).

Further outward, the gas is still irradiated by the central Trapezium stars, granting us the beautiful images of the Orion Nebula. The outward regions were dubbed the Extended Orion Nebula (EON, Güdel et al. 2008). It is, in fact, a closed circular structure of about 5 pc in diameter surrounding the bright Huygens Region, the latter being offset from its center. In the line of sight near the Trapezium stars in the Huygens Region, Orion’s Veil (O’Dell & Yusef-Zadeh 2000) is observed as a layer of (atomic and molecular) foreground gas at 1–3 pc distance from the blister of ionized gas that forms the bright Orion Nebula. H I and optical/UV absorption lines reveal multiple velocity components, some with velocities that link them to the expanding bubble part of the Veil² seen across the EON (Van der Werf et al. 2013; O’Dell 2018; Abel et al. 2019).

In the vicinity of the Orion Nebula, we find De Mairan’s Nebula (NGC 1982 or M43) just to the north of the Huygens Region, and the Running-Man Nebula (NGC 1973, 1975, and 1977) further up north. M43 hosts the central B0.5V star NU Ori and is shielded from ionizing radiation from the Trapezium cluster by the Dark Bay (O’Dell & Harris 2010; Simón-Díaz et al. 2011). NGC 1973, 1975, and 1977 possess as brightest star B1V star 42 Orionis in NGC 1977, which is the main ionizing source of that region (Peterson & Megeath 2008). The structure surrounding NGC 1973, 1975, and 1977 is dominated by the dynamics induced by 42 Orionis, hence, we will denote it by NGC 1977 only in the following.

The hot plasma filling stellar wind bubbles and the ionized gas of H II regions are both largely transparent for far-UV radiation. These non-ionizing photons are instead absorbed in the surrounding neutral gas, creating a warm layer of gas, the photodissociation region (PDR), which cools through atomic fine-structure lines (Hollenbach & Tielens 1999). The [C II] 158 μ m fine-structure line of ionized carbon is the dominant far-infrared (FIR) cooling line of warm, intermediate density gas ($T \sim 50$ – 300 K, $n \sim 10^3$ – 10^4 cm⁻³). It can carry up to 2% of the total FIR emission of the ISM, most of the FIR intensity arising from re-radiation of UV photons by interstellar dust grains. Velocity-resolved line observations provide a unique tool for the study of gas dynamics and kinematics. Velocity-resolved [C II] and [¹³C II] observations towards the Huygens Region/OMC1, an area of about $7.5' \times 11.5'$, were obtained and analyzed by Goicoechea et al. (2015). Here, we use a large-scale, $60' \times 80'$, study of velocity-resolved [C II] emission from the Orion Nebula M42, M43 and NGC 1973, 1975 and 1977³.

² We refer to Orion’s Veil as the Veil in short. We will refer to the large-scale expanding bubble as the Veil shell, being part of the same structure that covers the Huygens Region.

³ Two movie presentations of the velocity-resolved [C II] data are made available at <http://ism.strw.leidenuniv.nl/research.html#CII>.

¹ For a 3D journey through the Orion Nebula see https://www.jpl.nasa.gov/news/news.php?feature=7035&utm_source=i>Contact&utm_medium=email&utm_campaign=NASAJPL&utm_content=daily20180111-4

This paper is organized as follows. In Sect. 2, we review the observations that we used in the present study. In Sect. 3, we discuss the morphology of the shells associated with M 42, M 43, and NGC 1977 and derive gas masses and expansion velocities. Section 4 contains a discussion of the results presented in Sect. 3. We compare the observed shell kinematics with analytical models. We conclude with a summary of our results in Sect. 5.

2. Observations

2.1. [C II] observations

Velocity-resolved [C II] line observations towards the Orion Nebula complex, covering M 42, M 43 and NGC 1973, 1975, and 1977, were obtained during 13 flights in November 2016 and February 2017 using the 14-pixel high-spectral-resolution heterodyne array of the German Receiver for Astronomy at Terahertz Frequencies (upGREAT⁴, Risacher et al. 2016) onboard the Stratospheric Observatory for Infrared Astronomy (SOFIA). We produced a fully-sampled map of a 1.2 square-degree-sized area at an angular resolution of 16". The full map region was observed in the array on-the-fly (OTF) mode in 78 square tiles, each 435.6" wide. Each tile consists of 84 scan lines separated by 5.2", covered once in both x and y direction. Each scan line consists of 84 dumps of 0.3 s, resulting in a root-mean-square noise of $T_{\text{mb}} \approx 1.14$ K per pixel at a spectral resolution of 0.3 km s^{-1} . The original data at a native spectral resolution of 0.04 km s^{-1} were rebinned to 0.3 km s^{-1} channels to increase the signal-to-noise ratio (S/N). Ninety per cent of the total 2.2 million spectra required no post-processing, while most problematic spectra could be recovered using a spline baselining approach. A catalogue of splines is generated from data containing no astronomical signal. These splines could then be scaled to the astronomical data and more effectively remove the baselines than a polynomial fit. For a detailed description of the observing strategy and data reductions steps see Higgins et al. (in prep.).

2.2. CO observations

We also make use of ¹²CO $J=2-1$ (230.5 GHz) and ¹³CO $J=2-1$ (220.4 GHz) line maps taken with the IRAM 30 m radiotelescope (Pico Veleta, Spain) at a native angular resolution of 10.7". The central region ($1^\circ \times 0.8^\circ$) around OMC1 was originally mapped in 2008 with the HERA receiver array. Berné et al. (2014) presented the on-the-fly (OTF) mapping and data reduction strategies. In order to cover the same areas mapped by us in the [C II] line, we started to enlarge these CO maps using the new EMIR receiver and FFTS backends. These fully-sampled maps are part of the Large Program "Dynamic and Radiative Feedback of Massive Stars" (see the observing strategy and calibration in Goicoechea et al. 2020).

Goicoechea et al. (2020) provide details on how the old HERA and new EMIR CO maps were merged. Line intensities were converted from antenna temperature (T_A^*) scale to main-beam temperature (T_{mb}) using appropriate beam and forward efficiencies. Finally, and in order to properly compare with the velocity-resolved [C II] maps, we smoothed the CO(2-1) data to an angular resolution of 16". The typical root-mean-square noise level in the CO(2-1) map is 0.16 K in 0.4 km s^{-1} velocity resolution channels.

⁴ upGREAT is a development by the MPI für Radioastronomie (PI: R. Güsten) and KOSMA/Universität zu Köln, in cooperation with the MPI für Sonnensystemforschung and the DLR Institut für Optische Sensorsysteme.

2.3. Dust maps

In order to estimate the mass of the [C II]-traced gas in the expanding shells, we make use of FIR photometry obtained by *Herschel*. Lombardi et al. (2014) present a dust spectral energy distribution (SED) fit from *Herschel*/Photoconductor Array Camera and Spectrometer (PACS, Poglitsch et al. 2010) and Spectral and Photometric Imaging Receiver (SPIRE, Griffin et al. 2010) photometric images across a vast region of the Orion molecular cloud. However, they comment that the short-wavelength PACS $70 \mu\text{m}$ might be optically thick towards the dense molecular cores, hence they exclude it. Since we expect the expanding shell, we are mostly interested in, to mainly consist of optically thin, warm dust, we use the shorter-wavelength bands of PACS at 70, 100, and $160 \mu\text{m}$, tracing the warm dust; the longer-wavelength SPIRE bands at 250, 350, and $500 \mu\text{m}$, also included in the fit, are dominated by emission from cold (background) dust. We let the dust temperature T_d and the dust optical depth τ_{160} be free parameters, and fit SEDs using a modified blackbody for fixed grain emissivity index β :

$$I_\lambda = B(\lambda, T_d) \tau_{160} \left(\frac{160 \mu\text{m}}{\lambda} \right)^\beta. \quad (1)$$

We convolve and re-grid the PACS and SPIRE maps to the spatial resolution of the SPIRE $500 \mu\text{m}$ image, that is 36", at a pixel size of 14". SED fits to individual pixels are shown in Fig. A.1. We note that $\beta = 0$ results in the least residual in the PACS bands, but according to Hollenbach et al. (1991), at least $\beta = 1$ should be used. Often (e.g., in Goicoechea et al. (2015) for OMC1) $\beta = 2$ is adopted. The resulting dust temperature and dust optical depth vary considerably with β . Decreasing β from 2 to 1, decreases the dust optical depth by half, as does decreasing β from 1 to 0. The longer-wavelength SPIRE bands can only be fitted with $\beta = 1-2$. Since we use the conversion factors from τ to gas mass of Li & Draine (2001), we revert to $\beta = 2$ as suggested by their models. Lombardi et al. (2014) employ the β map obtained by Planck at 5' resolution, which amounts to $\beta \approx 1.6$. We note that τ_{160} is biased towards the warm dust, which is beneficial for our purposes. We could have constrained the SED fits to the three PACS bands, using $\beta = 2$. This leaves the dust temperature and the dust optical depth in the shells mostly unchanged. The only exception is the southern part of the limb-brightened Veil shell, where the dust optical depth turns out to be 30% lower. In addition, the dust optical depth towards the molecular background is reduced by half. From the dust optical depth τ_{160} , we can compute the gas column density:

$$N_{\text{H}} \approx \frac{100 \tau_{160}}{\kappa_{160} m_{\text{H}}} \approx 6 \times 10^{24} \text{ cm}^{-2} \tau_{160}, \quad (2)$$

where we have used a gas-to-dust mass ratio of 100 and assumed a theoretical absorption coefficient $\kappa_{160} \approx 10.5 \text{ cm}^2 \text{ g}^{-1}$ appropriate for $R_V = 5.5$ (Weingartner & Draine 2001).

To estimate the contribution of emission from very small grains (VSGs) in the $70 \mu\text{m}$ band, we compare the latter with the *Spitzer*/Multiband Imaging Photometer (MIPS) $24 \mu\text{m}$ image. VSGs in PDRs are stochastically heated and obtain temperatures that are higher than that of larger grains. In the shells of the Orion Veil, M 43, and NGC 1977, their contribution is small. In the bubble interiors, however, the emission from hot dust tends to dominate: dust in these H II region becomes very warm due to absorption of ionizing photons and resonantly trapped Ly α photons and radiates predominantly at $24 \mu\text{m}$ (Salgado et al. 2016). For dust in the PDR, the observed flux at wavelength shorter

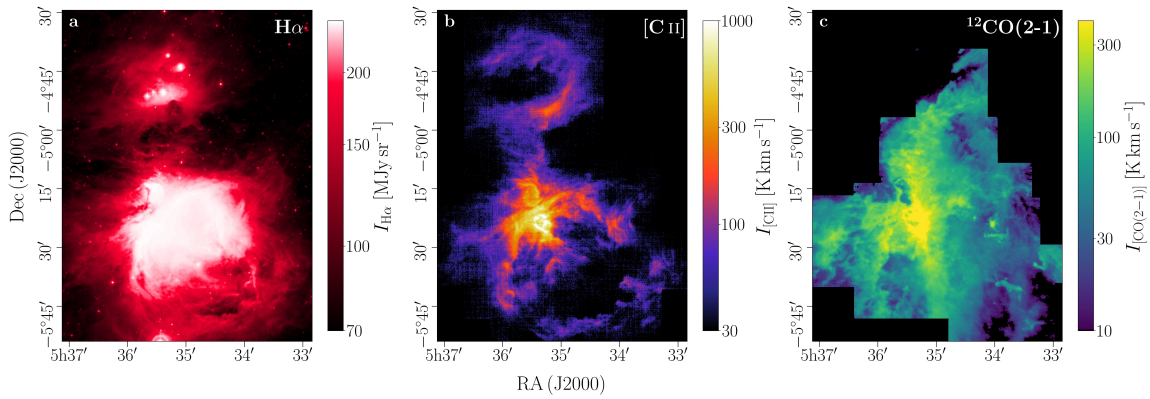


Fig. 1. Overview of the Orion Nebula (M 42), M 43, and NGC 1973, 1975, and 1977 in different wavelengths. *Left:* DSS2 $H\alpha$ emission (ESO Archive). *Center:* [C II] line-integrated emission (Pabst et al. 2019). *Right:* line-integrated $^{12}\text{CO}(2-1)$ emission (Berné et al. 2014; Goicoechea et al. 2020). $H\alpha$ emission stems from the ionized gas ($T \sim 10^4$ K), the [C II] line is emitted by mostly neutral gas ($T \sim 100$ K), whereas CO traces the molecular gas ($T \sim 30$ K). M 42 and M 43 have a substantial amount of molecular gas in the background, while NGC 1977 seems to be devoid of it (the coverage of the CO map is not sufficient, however, see discussion of the expansion characteristics below). All three regions comprise ionized gas within their neutral limb-brightened shells.

than $24\mu\text{m}$ is due to emission by fluctuating grains and PAH molecules and we defer this analysis to a future study.

2.4. $H\alpha$ observations

We make use of three different $H\alpha$ observations: the Very Large Telescope (VLT)/Multi Unit Spectroscopic Explorer (MUSE) image taken of the Huygens Region (Weilbacher et al. 2015), the image taken by the Wide Field Imager (WFI) on the European Southern Observatory (ESO) telescope at La Silla of the surrounding EON (Da Rio et al. 2009), and a ESO/Digitized Sky Survey 2 (DSS-2) image (red band) covering the entire area observed in [C II]. The DSS-2 image is saturated in the inner EON, which is basically the coverage of the WFI image. We use the MUSE image to calibrate the WFI image in units of MJy sr^{-1} with a log fit of the correlation. The units of the MUSE observations are given as $10^{-12} \text{ erg s}^{-1} \text{ cm}^{-3}$, which we convert to MJy sr^{-1} with the central wavelength $\lambda \simeq 656.3 \text{ nm}$ and a pixel size of $0.2''$. We in turn use the thus referenced WFI image to calibrate the DSS-2 image with a fit of the form $y = a(1 - \exp(-bx))$, where x , y are the two intensities scaled by the fit parameters. To calculate the surface brightness from the spectral brightness we use a $\Delta\lambda = 0.85 \text{ \AA}$, that is $I = I_\lambda \Delta\lambda = I_\nu \Delta\nu$.

We only use the thus calibrated DSS-2 image in NGC 1977 for quantitative analysis. The $H\alpha$ surface brightness in the EON is largely due to scattered light from the bright Huygens Region (O'Dell & Harris 2010). Also $H\alpha$ emission in M 43 has to be corrected for a contribution of scattered light from the Huygens Region (Simón-Díaz et al. 2011).

We correct for extinction towards NGC 1977, using $R_V = 5.5$, suitable for Orion. The reddening is $E(B-V) = 0.08$ (Knyazeva & Kharitonov 1998). For M 43, the reddening is $E(B-V) = 0.49$ (Megier et al. 2005). Extinction towards M 42 was studied by O'Dell & Yusef-Zadeh (2000), for example, and more recently by Weilbacher et al. (2015).

3. Analysis

3.1. Global morphology

From the comparison of the three gas tracers in Fig. 1, we see that [C II] emission stems from different structures than either $H\alpha$,

tracing the ionized gas, or $^{12}\text{CO}(2-1)$, tracing the cold molecular gas. In fact, from Fig. 1 in Pabst et al. (2019) we conclude that it stems from the same regions as the warm-dust emission and PAH emission. We can quantify this by correlation plots of the respective tracers (Pabst et al., in prep.). We clearly see bubble-like structures in [C II], that are limb-brightened towards the edges. The southern red circle in Fig. 2 indicates the outlines of the bubble of M 42. We note that the Trapezium stars, causing the bubble structure, are offset from the bubble center; in fact, they seem to be located at the northern edge of the bubble. We estimate a bubble radius of $r \simeq 2.7 \text{ pc}$. However, when taking into account the offset of the Trapezium stars, the gas at the southern edge of the bubble is some 4 pc from the stars. The geometry of the bubble indicates that there is a significant density gradient from the north, where the Trapezium stars are located, to the south, the ambient gas there being much more dilute.

In M 43, the star NU Ori is located at the center of the surrounding bubble. 42 Orionis in NGC 1977 is slightly offset from the respective bubble center (cf. Fig. 2). Both bubbles are filled with ionized gas as observed in $H\alpha$ emission (cf. Fig. 1) as well as radio emission (Subrahmanyan et al. 2001). In the main part of this section, we derive the mass, physical conditions and the expansion velocity of the expanding shells associated with M 42, M 43, and NGC 1977.

3.2. The expanding Veil shell – M 42

3.2.1. Geometry, mass and physical conditions

The prominent shell structure of the Orion Nebula is surprisingly symmetric, although it is offset from the Trapezium cluster. From the pv diagrams (cf. Sect. 3.2.2 and Appendix C), we estimate its geometric center at $(\Delta\alpha, \Delta\delta) = (-520'', -550'')$ and its radius with $r = 1360'' = 0.38 \text{ deg}$, which corresponds to $r \simeq 2.7 \text{ pc}$ at the distance of the Orion Nebula; the geometric center of the bubble has a projected distance of 1.5 pc from the Trapezium cluster. Hence, the gas in the southern edge of the bubble is about 4 pc away from the Trapezium stars, whereas to the north the bubble outline is more ellipsoid and the gas in the shell is at only 0.5 pc distance.

The limb-brightened shell of the expanding Veil bubble is mainly seen in the velocity range (with respect to the Local

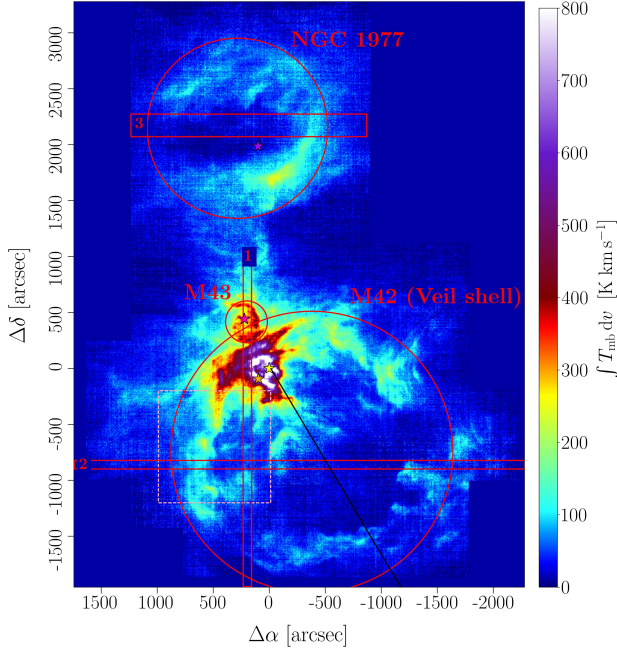


Fig. 2. [C II] line-integrated intensity from the Orion Nebula (M42), M43, and NGC 1977. The red rectangles 1 and 2 indicate the positions of the pv diagrams shown in Figs. 5 (horizontal) and 8 (vertical). Rectangle 3 indicates the position of the pv diagram shown in Fig. 17. The red circles delineate the approximate extent of the expanding bubbles of gas that are the Veil shell, M43, and NGC 1977, and within which the respective masses and luminosities are computed. The light-red dashed rectangle circumscribes the area of the eastern bright arm shown in Figs. B.1 and B.2. The black line indicates the position of the line cut in Fig. 4. The stars mark the position of θ^1 Ori C (yellow), θ^2 Ori A (orange), NU Ori (pink), and 42 Orionis (purple). Unless noted otherwise, all coordinate offsets are given with respect to the position of θ^1 Ori C, $(\alpha, \delta) = (5h35'16.46'', -5^\circ23'22.85'')$.

Standard of Rest (LSR)) $v_{\text{LSR}} = 5\text{--}8 \text{ km s}^{-1}$. The emission from the bubble itself can be found down to $v_{\text{LSR}} \approx -7 \text{ km s}^{-1}$ (cf. Sect. 3.2.2). The bright main component, that originates from the surface of the background molecular cloud, lies at $v_{\text{LSR}} \approx 8 \text{ km s}^{-1}$; in the bright Huygens Region significant emission extends up to $v_{\text{LSR}} \sim 15 \text{ km s}^{-1}$. Here, we also detect the $^{13}\text{C II}$ $F = 2\text{--}1$ line in individual pixels, corresponding to gas moving at $v_{\text{LSR}} \sim 8 \text{ km s}^{-1}$ (see previous detections of $^{13}\text{C II}$ lines in Boreiko & Betz 1996; Ossenkopf et al. 2013; Goicoechea et al. 2015).

Figure 3 shows the average [C II] spectrum towards the Veil shell without OMC1 and the ISF. The $^{13}\text{C II}$ $F = 2\text{--}1$ line, one of the three $^{13}\text{C II}$ fine-structure lines, that is shifted by 11.2 km s^{-1} with respect to the $^{12}\text{C II}$ line, is marginally detected. We estimate the detection significance over the integrated line from the fit errors at 5σ . From the $^{13}\text{C II}$ $F = 2\text{--}1$ line, we can compute the [C II] optical depth $\tau_{[\text{C II}]}$ and the excitation temperature T_{ex} :

$$\frac{1 - \exp(-\tau_{[\text{C II}]})}{\tau_{[\text{C II}]}} \approx \frac{0.625 T_{\text{P}}(^{12}\text{C II})}{[^{12}\text{C}/^{13}\text{C}] T_{\text{P}}(^{13}\text{C II}, F = 2 - 1)}, \quad (3)$$

$$T_{\text{ex}} = \frac{91.2 \text{ K}}{\ln\left(1 + \frac{91.2 \text{ K}(1 - \exp(-\tau_{[\text{C II}]})}{T_{\text{P}}(^{12}\text{C II}) + T_{\text{c}}}\right)}, \quad (4)$$

where $^{12}\text{C}/^{13}\text{C} \sim 67$ is the isotopic ratio for Orion (Langer & Penzias 1990) and 0.625 is the relative strength of the $^{13}\text{C II}$

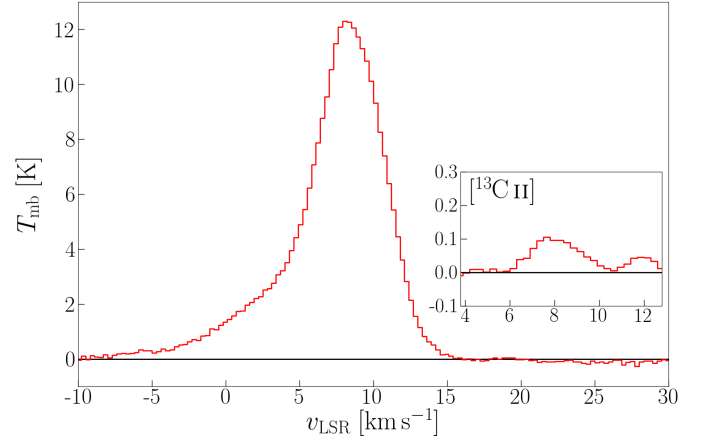


Fig. 3. Average [C II] spectrum towards the Veil shell without OMC1 and ISF. The inlaid panel shows the residual of the spectrum, in the systemic velocity of the $^{13}\text{C II}$ $F = 2 - 1$ line, after subtracting the $^{12}\text{C II}$ fit. The $^{12}\text{C II}$ line can be fitted by two Gaussians with $T_{\text{P}} \approx 11.2 \pm 0.3 \text{ K}$, $v_{\text{p}} \approx 8.8 \pm 0.1 \text{ km s}^{-1}$, $\Delta v_{\text{FWHM}} \approx 5.0 \pm 0.1 \text{ km s}^{-1}$ and $T_{\text{P}} \approx 2.3 \pm 0.1 \text{ K}$, $v_{\text{p}} \approx 4.0 \pm 0.4 \text{ km s}^{-1}$, $\Delta v_{\text{FWHM}} \approx 9.3 \pm 0.5 \text{ km s}^{-1}$; the $^{13}\text{C II}$ $F = 2 - 1$ component is fitted by a Gaussian with $T_{\text{P}} \approx 0.11 \pm 0.02 \text{ K}$, $v_{\text{p}} \approx 8.2 \pm 0.3 \text{ km s}^{-1}$, $\Delta v_{\text{FWHM}} \approx 2.1 \pm 0.6 \text{ km s}^{-1}$. The main line could also be fitted with three Gaussian components, but we compare the respective combined peak temperatures of the $^{12}\text{C II}$ and $^{13}\text{C II}$ line for a first-order estimate of the excitation conditions.

$F = 2 - 1$ line (Ossenkopf et al. 2013); $T_{\text{c}} = \frac{91.2 \text{ K}}{\exp(91.2 \text{ K}/T_{\text{d}}) - 1}$ is the continuum brightness temperature of the dust background (Goicoechea et al. 2015). In general, $T_{\text{P}}(^{12}\text{C II}) \gg T_{\text{c}}$ in the limb-brightened shells. The measured peak temperatures yield $\tau_{[\text{C II}]} \approx 0.1$ and $T_{\text{ex}} \approx 144 \text{ K}$ for the averaged spectrum. We obtain an average C^+ column density of $N_{\text{C}^+} \approx 3 \times 10^{17} \text{ cm}^{-2}$. These results have to be interpreted with caution, since we average over a large region with very different conditions (G_0 , n) and the signal is likely dominated by the bright eastern Rim of the Veil shell (see Appendix B for a discussion thereof). Also, baseline removal for the $^{13}\text{C II}$ line is problematic. From the dust optical depth, we estimate a much larger column density towards the Veil shell, $N_{\text{C}^+} \gtrsim 10^{18} \text{ cm}^{-2}$.

If we assume the [C II] emission from the limb-brightened shell to be (marginally) optical thick, that is $\tau_{[\text{C II}]} \gtrsim 1$, we can also estimate the excitation temperature from the peak temperature of the $^{12}\text{C II}$ spectra by Eq. (4). We obtain excitation temperatures of $T_{\text{ex}} \approx 100 \text{ K}$ in the Eastern Rim (and similar gas temperatures), and $T_{\text{ex}} \approx 50 \text{ K}$ in the far edge of the shell. Here, the density presumably is somewhat lower, resulting in a higher gas temperature. The gas (or kinetic) temperature is given by:

$$T_{\text{gas}} = \frac{T_{\text{ex}}}{1 - \frac{T_{\text{ex}}}{91.2 \text{ K}} \ln\left(1 + \frac{n_{\text{cr}}}{n}\right)}, \quad (5)$$

where $n_{\text{cr}} \approx 3 \times 10^3 \text{ cm}^{-3}$ is the critical density for $\text{C}^+\text{-H}$ collisions (Goldsmith et al. 2012; Pabst et al. 2017). With the density estimates below, the gas temperature in the southern Veil shell is $T_{\text{gas}} \approx 70\text{--}125 \text{ K}$.

From the dust SEDs, Pabst et al. (2019) estimate $M \approx 2600_{-900}^{+800} M_{\odot}$ for the mass of the gas in the Veil shell after accounting for projection effects. This is in good agreement with their mass estimate from the $^{13}\text{C II}$ line in the brightest parts of the shell. The bright eastern part of the shell, however, might not be representative of the entire limb-brightened shell of the Veil shell. From a line cut through this Eastern Rim

(Fig. B.4), we estimate a density of $n \simeq 9 \times 10^3 \text{ cm}^{-3}$ from the spatial separation of the peaks in [C II] and CO emission (see Appendix B), assuming an A_V of 2 for the C^+/CO transition and $N_{\text{H}}/A_V \simeq 2 \times 10^{21} \text{ cm}^{-2}$ (Bohlin et al. 1978). Although continuously connected to the limb-brightened Veil shell in space and velocity, this Eastern Rim might be a carved-out structure in the background molecular cloud, as has been argued from the presence of foreground scattered light from the Trapezium stars (O'Dell & Goss 2009). We note that the [C II] emission from the expanding shell connected to the Eastern Rim is confined to within the Rim, supporting the view that the Eastern Rim is a static confinement of the expanding bubble.

Morphologically, the Eastern Rim fits well in with the rest of the Veil shell, following its curvature well and forming one, seemingly coherent structure. In contrast, there is no connection to the ISF that spans up the dense core of the Orion molecular cloud in the submillimeter maps (cf. Fig. 1). It is then hard to conceive that this part of the nebula is a fortuitous coincidence of the expanding Veil shell encountering a background or foreground molecular cloud structure. On the other hand, the channel maps do not reveal the shift of the shell with increasing velocity in the Eastern Rim that are the signature of an expanding shell in the other parts of the Veil shell (cf. Fig. 7). Excluding the area associated directly with the dense PDR around the Trapezium (indicated by the circle in Extended Data Fig. 8 in Pabst et al. 2019), analysis of the dust SED yields $M \simeq 2600 M_{\odot}$ for the mass of the Veil shell. If we also exclude the Eastern Rim, this drops to $M \simeq 1500 M_{\odot}$.

From the visual extinction towards the Trapezium cluster, $A_V \simeq 1.8$ (O'Dell & Goss 2009), corresponding to a hydrogen column density of $N_{\text{H}} \simeq 3.6 \times 10^{21} \text{ cm}^{-2}$, the mass of the half-shell can be estimated as $M \simeq 2\pi r^2 N_{\text{H}} \mu m_{\text{H}}$, where $\mu = 1.4$ is the mean molecular weight. With $r \simeq 2.5 \text{ pc}$, this gives $M \simeq 1600 M_{\odot}$. From H_2 and carbon line observations towards the Trapezium cluster, Abel et al. (2016) estimate a density of $n \simeq 2.5 \times 10^3 \text{ cm}^{-3}$ and a thickness of the large-scale Veil component B of $d \simeq 0.4 \text{ pc}$, resulting in a visual extinction of $A_V \simeq 1.5$. In a new study of optical emission and absorption lines plus [C II] and H I line observations, Abel et al. (2019) determine $n \simeq 1.6 \times 10^3 \text{ cm}^{-3}$ for the density in the Veil towards the Trapezium cluster, their Component III(B). However, the central part of the Veil might not be representative of the entire Veil shell, since the [C II] emission from the Veil in the vicinity of the Trapezium stars is less distinct than in the farther parts of the Veil shell, suggesting somewhat lower column density in the central part. The visual extinction, as seen by MUSE (Weilbacher et al. 2015), varies across the central Orion Nebula and decreases to only $A_V \simeq 0.7$ to the west of the Trapezium cluster. Using this value reduces the mass estimate of the Veil shell to $M \sim 600 M_{\odot}$.

X-ray observations of the hot plasma within the EON indicate varying extinction due to the foreground Veil shell. Güdel et al. (2008) derive an absorbing hydrogen column density of $N_{\text{H}} \simeq 4 \times 10^{20} \text{ cm}^{-2}$ towards the northern EON and $N_{\text{H}} \leq 10^{20} \text{ cm}^{-2}$ towards the southern X-ray emitting region. Assuming again $T_{\text{ex}} \simeq 50 \text{ K}$, these column densities correspond to [C II] peak temperatures of $T_{\text{p}} \simeq 2 \text{ K}$ and $T_{\text{p}} \simeq 0.5 \text{ K}$, respectively, which would be below the noise level of our observations. Yet, we do detect the [C II] Veil shell towards these regions (cf. Figs. C.1 and C.2). From the lack of observable X-rays towards the eastern EON and the more prominent [C II] Veil shell in this region, we suspect that the absorbing column of neutral gas is higher in the eastern Veil shell.

With the MUSE estimate for the column density, we can estimate the density and check for consistency with our [C II]

observations. With a shell thickness of $d \simeq 0.3 \text{ pc}$ and a visual extinction of $A_V \simeq 0.7$, we estimate a density in the Veil shell of $n \simeq 1.5 \times 10^3 \text{ cm}^{-3}$. We will use this density estimate in the following, but we note that we consider this a lower limit as the density estimate from a typical dust optical depth, $\tau_{160} \simeq 2 \times 10^{-3}$, in the southern Veil shell and a typical line of sight, $l \simeq r/2$, gives $n \simeq 4 \times 10^3 \text{ cm}^{-3}$. However, from the lack of detectable wide-spread CO emission from the Veil shell, also in the southern limb-brightened shell, we can set an upper limit for the visual extinction of $A_V \sim 2$, equivalent to a gas column of $N_{\text{H}} \sim 4 \times 10^{21} \text{ cm}^{-2}$ (Goicoechea et al. 2020).

With a shell thickness of $d \simeq 0.3 \text{ pc}$ and a density of $n \simeq 1.5 \times 10^3 \text{ cm}^{-3}$, the shell has a radial C^+ column density of $N_{\text{C}^+} \simeq 2 \times 10^{17} \text{ cm}^{-2}$. Adopting this latter value and an excitation temperature of $T_{\text{ex}} = 50 \text{ K}$, the calculated [C II] optical depth, given by:

$$\tau_{[\text{C II}]} = \frac{A\lambda^3}{4\pi b} N_{\text{C}^+} \frac{\exp\left(\frac{\Delta E}{k_{\text{B}} T_{\text{ex}}}\right) - 1}{\exp\left(\frac{\Delta E}{k_{\text{B}} T_{\text{ex}}}\right) + 2}, \quad (6)$$

in the shell seen face-on is $\tau_{[\text{C II}]} \simeq 0.4$, with a line width of $\Delta v_{\text{FWHM}} = 2\sqrt{\ln 2} b \simeq 4 \text{ km s}^{-1}$. The expected peak temperature then,

$$T_{\text{p}} = \frac{91.2 \text{ K}(1 - \exp(-\tau_{[\text{C II}]}))}{\exp\left(\frac{91.2 \text{ K}}{T_{\text{ex}}}\right) - 1}, \quad (7)$$

is $T_{\text{p}} \simeq 6 \text{ K}$, which is in reasonably good agreement with the peak temperatures of the narrow expanding components in spectra in Fig. 6.

We can also calculate the mass of the [C II]-emitting gas from the luminosity of the shell, $L_{[\text{C II}]} \simeq 170 L_{\odot}$ in the limb-brightened Veil shell, assuming that the line is effectively optically thin. By

$$M = \frac{\mu m_{\text{H}}}{\mathcal{A}_{\text{C}} A \Delta E} \left(\frac{g_{\text{l}}}{g_{\text{u}}} \exp\left(\frac{\Delta E}{k_{\text{B}} T_{\text{ex}}}\right) + 1 \right) L_{[\text{C II}]}, \quad (8)$$

where $\mathcal{A}_{\text{C}} \simeq 1.6 \times 10^{-4}$ is the carbon gas-phase abundance (Sofia et al. 2004), $A \simeq 2.3 \times 10^{-6} \text{ s}^{-1}$ the Einstein coefficient for spontaneous emission, $\Delta E/k_{\text{B}} \simeq 91.2 \text{ K}$ the level separation of the two levels with statistical weights $g_{\text{l}} = 2$ and $g_{\text{u}} = 4$, we obtain $M \simeq 680 M_{\odot}$, assuming an excitation temperature of $T_{\text{ex}} = 50 \text{ K}$. As we expect the line to be (marginally) optically thick in the limb-brightened shell, $\tau_{[\text{C II}]} \simeq 1-2$, this value constitutes a lower limit of the shell mass. Correcting with this [C II] optical depth would yield a mass estimate of at least $M \simeq 1100 M_{\odot}$. For further analysis we will use the mass estimate from the dust optical depth, where we have subtracted the mass of the Eastern Rim, $M \simeq 1500 M_{\odot}$. This mass estimate is robust when considering only the PACS bands in the SED, reducing contamination by cold background gas. We recognize that the column density of the shell is highly variable and is lowest in the foreground shell. This is as expected given the strong pressure gradient from the molecular cloud surface towards us (cf. Sect. 4.1).

We judge that the large-scale arc-structured [C II] line emission mainly stems from the outer dense neutral shell indeed, rather than from the contained ionized gas. Evidence for this is the rather small line width where there is a significant signal, which is comparable to the line width of the main component from the neutral surface layer of the molecular cloud ($\Delta v_{\text{FWHM}} \simeq 3-4 \text{ km s}^{-1}$, cf. Fig. 6). If the [C II] line originated from the hot ($T \sim 10^4 \text{ K}$) ionized gas, we would expect it to be broader,

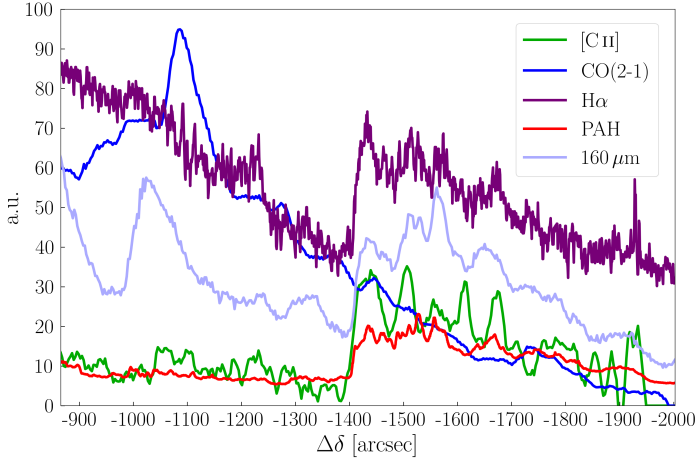


Fig. 4. Line cut through the southwest of the Veil shell, indicated in Fig. 2. The onset of the shell is marked by a steep increase in all tracers, except CO, at $\Delta\delta \approx -1400''$. With a line angle of 30° with respect to the vertical axis, this is at a distance of 3.25 pc from the Trapezium stars.

$\Delta v_{\text{FWHM}} \sim 10 \text{ km s}^{-1}$, as observed in the H II region bordering the Horsehead Nebula (Pabst et al. 2017). Where the signal from the expanding shell is weak, we indeed observe such broad lines, hence part of the shell might still be ionized (see Sect. 4.4 for a discussion of the ionization structure of wind-blown bubbles). The limb-brightened shell is also visible in $\text{H}\alpha$, indicating that the surface is ionized. This is also illustrated by the line cut in Fig. 4, where the onset of the shell is marked by a steep increase in all tracers except CO. The relative lack of CO indicates low extinction of FUV photons within the southern shell and gives an upper limit on the density in this part, $n \lesssim 3 \times 10^3 \text{ cm}^{-3}$. From the correlation with other (surface) tracers ($[\text{C II}]$, $8 \mu\text{m}$, $160 \mu\text{m}$) along the line cut we conclude that the shell has a corrugated surface structure, as there are multiple emission peaks in these tracers behind the onset of the shell.

The broader lines ($\Delta v_{\text{FWHM}} > 5 \text{ km s}^{-1}$) we observe where the shell arc is barely visible, agree with an estimation of the expected $[\text{C II}]$ emission from ionized gas in the shell. Here, we have (Pabst et al. 2017):

$$I_{[\text{C II}]} \approx 10 \text{ K km s}^{-1} \frac{n_e}{10^2 \text{ cm}^{-3}} \frac{l}{1 \text{ pc}}, \quad (9)$$

which is, with an electron density of $n_e \sim 50\text{--}100 \text{ cm}^{-3}$ (O'Dell & Harris 2010) and a line of sight of $l \sim 0.3 \text{ pc}$, what we find in the spectra from the pv diagram in Fig. 6. We do not expect much $[\text{C II}]$ emission from the inner region of the EON, since the dominant ionization stage of carbon in the vicinity of a O7 star is C^{2+} .

3.2.2. Expansion velocity

Persistent arc structures observed in position-velocity (pv) diagrams are the signature of bubbles that form in the ISM. By the aid of such diagrams one can estimate the expansion velocity of the associated dense shell. The pv diagrams for the Veil shell reveal the presence of a half shell. Figure 5 shows one such pv diagram as an example. Other cuts are shown in Appendix C. Pabst et al. (2019) estimate an expansion velocity of $v_{\text{exp}} \approx 13 \text{ km s}^{-1}$ for this half shell. This value is consistent with Gaussian fits to single (averaged) spectra taken from the pv diagram where this is possible (Fig. 6).

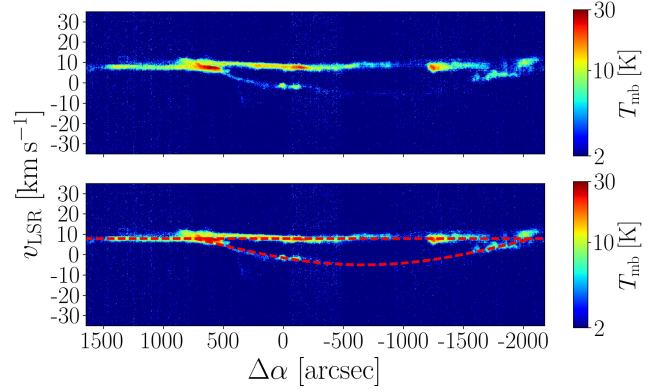


Fig. 5. $[\text{C II}]$ pv diagram along horizontal position cut 2 indicated in Fig. 2 ($\Delta\delta = -907''\text{--}(-831'')$). The lower panel shows the same cut with the arc structure for an expansion velocity of 13 km s^{-1} on a background velocity of 8 km s^{-1} (red dashed lines).

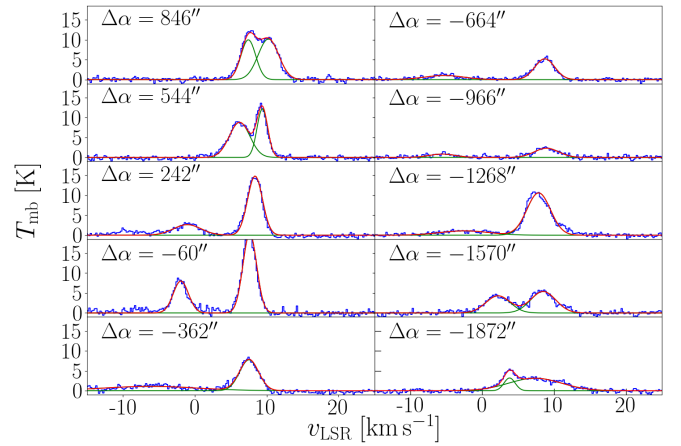


Fig. 6. $[\text{C II}]$ spectra in the Veil shell taken from pv diagram in Fig. 5 with Gaussian fits. Spectra at $\Delta\alpha = -362''$ to $\Delta\alpha = -1268''$ are averaged over $151'' \times 75.5''$ in order to improve the signal-to-noise ratio of the faint shell component to be fitted, others are averaged over $75.5'' \times 75.5''$. Coordinate offsets indicate the lower left-hand corner of the rectangle over which the spectra are averaged; $\Delta\delta = -907''$. The fit parameters are given in Table 1.

It is important to note that the bubble shell traced by $[\text{C II}]$ emission expands in one direction only, which is towards us. Towards the back, the gas is confined by the background molecular cloud hindering rapid expansion. The prominent 8 km s^{-1} emission originates from this dense background gas.

An alternative way to estimate the expansion velocity of the bubble is from channel maps of this region. With increasing v_{LSR} , the limb-brightened shell filament of M 42 is observed to move outward, away from the Trapezium stars, as can be seen from Fig. 7. The projected geometry of the filaments in different channels provides an estimate of v_{exp} . However, this only works well in the bright eastern arm of the shell, the so-called Rim, which is comparatively narrow (cf. Appendix B, Figs. B.1 and B.2). In other parts of the limb-brightened shell, the south and west, the filaments in different velocities do not line up consistently. To the north of the Trapezium stars, we do not see outward expansion at all. From these alternative methods (fitting Gaussians to single spectra, outlines of the limb-brightened shell) we find values agreeing with those computed above from the pv diagram, $v_{\text{exp}} \approx 10\text{--}15 \text{ km s}^{-1}$. Also the majority of pv diagrams shown

Table 1. Gaussian fit parameters of spectra in Fig. 6.

$\Delta\alpha$	Comp.	T_p [K]	v_p [km s ⁻¹]	Δv_{FWHM} [km s ⁻¹]
846''	1	10.2 ± 0.2	10.2 ± 0.1	3.4 ± 0.2
846''	2	10.0 ± 0.5	7.4 ± 0.1	2.4 ± 0.1
544''	1	12.2 ± 0.2	9.4 ± 0.1	1.7 ± 0.1
544''	2	8.8 ± 0.2	6.2 ± 0.1	3.4 ± 0.1
242''	1	14.8 ± 0.2	8.4 ± 0.1	2.4 ± 0.1
242''	2	2.6 ± 0.2	-1.1 ± 0.1	4.5 ± 0.3
-60''	1	20.0 ± 0.3	7.6 ± 0.1	2.2 ± 0.1
-60''	2	8.0 ± 0.2	-2.0 ± 0.1	2.5 ± 0.1
-362''	1	7.8 ± 0.2	7.5 ± 0.1	3.1 ± 0.1
-362''	2	1.1 ± 0.1	-6.2 ± 0.4	15.4 ± 1.2
-664''	1	5.2 ± 0.1	8.7 ± 0.1	3.3 ± 0.1
-664''	2	1.0 ± 0.1	-5.3 ± 0.3	6.4 ± 0.6
-966''	1	2.3 ± 0.2	8.9 ± 0.1	4.0 ± 0.3
-966''	2	0.8 ± 0.2	-5.5 ± 0.3	4.2 ± 0.7
-1268''	1	10.6 ± 0.2	7.9 ± 0.1	3.9 ± 0.1
-1268''	2	1.1 ± 0.1	-2.5 ± 0.3	8.0 ± 0.8
-1570''	1	5.4 ± 0.2	8.5 ± 0.1	4.1 ± 0.2
-1570''	2	4.3 ± 0.2	2.2 ± 0.1	4.0 ± 0.2
-1872''	1	3.1 ± 0.1	7.4 ± 0.2	8.7 ± 0.3
-1872''	2	3.2 ± 0.2	3.8 ± 0.1	1.8 ± 0.2

Notes. The expanding Veil shell is captured in component 2.

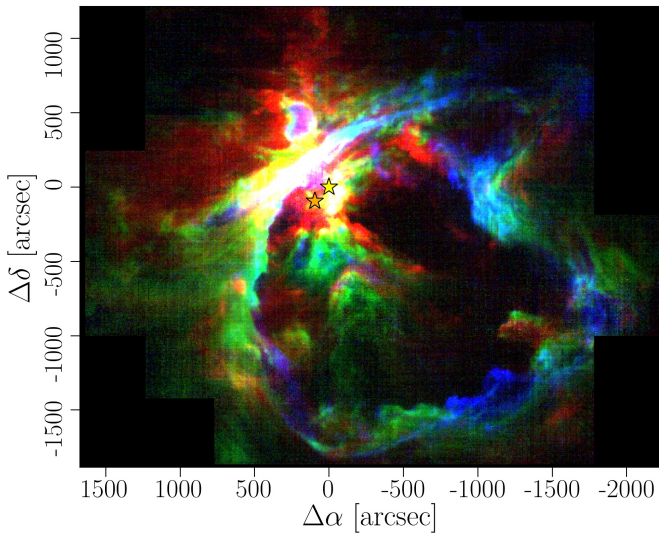


Fig. 7. Three-color image of velocity channels towards M42 and M43. Blue is the velocity channel $v_{\text{LSR}} = 4\text{--}5\text{ km s}^{-1}$, green $v_{\text{LSR}} = 6\text{--}7\text{ km s}^{-1}$, and red $v_{\text{LSR}} = 9\text{--}10\text{ km s}^{-1}$. With increasing v_{LSR} , the limb-brightened Veil shell filament is displaced outward, away from the bubble center. The gas of M43 that is expanding towards us can be observed in the blue channel; the limb-brightened shell of M43 has higher v_{LSR} .

in Figs. C.1 and C.2 are consistent with an overall expansion velocity of $v_{\text{exp}} \approx 13\text{ km s}^{-1}$.

Figure 8 compares the velocity structures of [C II], $^{12}\text{CO}(2-1)$, $^{13}\text{CO}(2-1)$, and H I along a vertical cut at

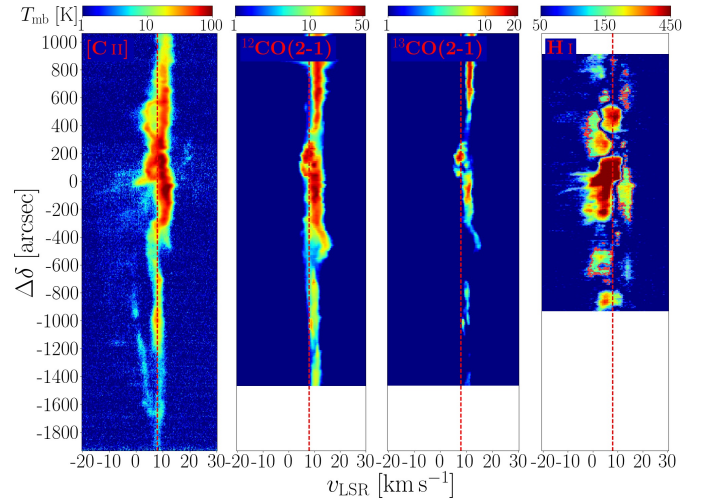


Fig. 8. PV diagrams along vertical position cut 1 indicated in Fig. 2 ($\Delta\alpha = 167''\text{--}242''$) in [C II], $^{12}\text{CO}(2-1)$, $^{13}\text{CO}(2-1)$ (Berné et al. 2014; Goicoechea et al. 2020), and H I (Van der Werf et al. 2013).

$\Delta\alpha = 167''\text{--}242''$. This figure illustrates the complex dynamics in the region of the Orion Nebula and contrasts the various kinematic structures in the different tracers. It gives an impression of the variety of emission structures and the potential synergies between the four data sets. The cut shows arc structures close to the central region (Huygens Region) that coincide with structures detected in H I and discussed in Van der Werf et al. (2013). Also, the shell surrounding M43 is distinctly visible (cf. Fig. 12). We note that to the north the bubble-like arc of the Veil shell is disrupted by apparently violent gas dynamics in that region, even far to the west of the Huygens Region. Closer examination of pv diagrams in this region reveal multiple arcs indicative of bubble structures (see Appendix C for all pv diagrams through the Veil shell). South of OMC1, the observed difference in velocity ($\sim 1\text{ km s}^{-1}$) between the [C II] background and the molecular cloud as traced by CO is typical for the advection flow through the PDR (Tielens 2010, Chap. 12). From our analysis, we conclude that the systematic uncertainty of the mass estimate are of the order of 50%, systematic uncertainties of the estimates of the extent of the shell and of the expansion velocity are about 30%.

3.3. M43

3.3.1. Geometry, mass and physical conditions

The nebula M43 hosts the central star NU Ori, which is located approximately at the geometrical center of the limb-brightened shell. The shell radius is $r \approx 150'' \approx 0.3\text{ pc}$ with a thickness of $\Delta r \approx 0.05\text{ pc}$. Figure 9 shows a three-color image of M43. $\text{H}\alpha$ stems from the center of M43, constrained by a thin shell of [C II] and CO in the east and north. To the south lies the massive bulk of OMC1. The H II region of M43 appears as a region of higher dust temperature, the shell is distinctly visible in [C II], IRAC $8\mu\text{m}$ emission, FIR emission from warm dust (cf. Fig. 1 in Pabst et al. 2019), and CO. The limb-brightened shell reveals the structure of a PDR with $8\mu\text{m}$ PAH emission, [C II] emission, and $160\mu\text{m}$ warm dust emission originating at the inner, illuminated side while the CO emission originates from deeper within the shell (Fig. 10). M43 is located just eastwards of the ridge of the molecular ISF, whose illuminated, [C II] emitting outliers form the background against which the half-shell expands.

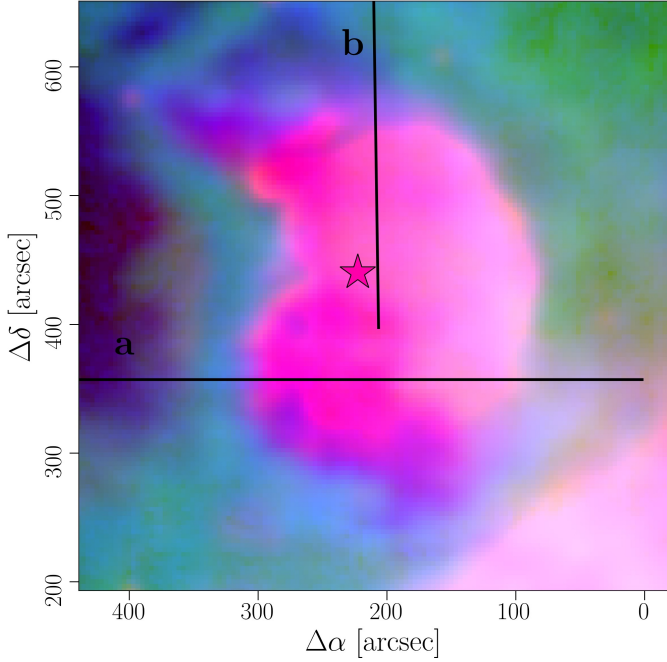


Fig. 9. Three-color image of M 43. Red is H α emission from the ionized gas, green is line-integrated CO(2–1) emission from molecular gas, and blue is the [C II] line-integrated intensity, tracing the neutral gas. The line cuts in Fig. 10 are taken along lines a and b.

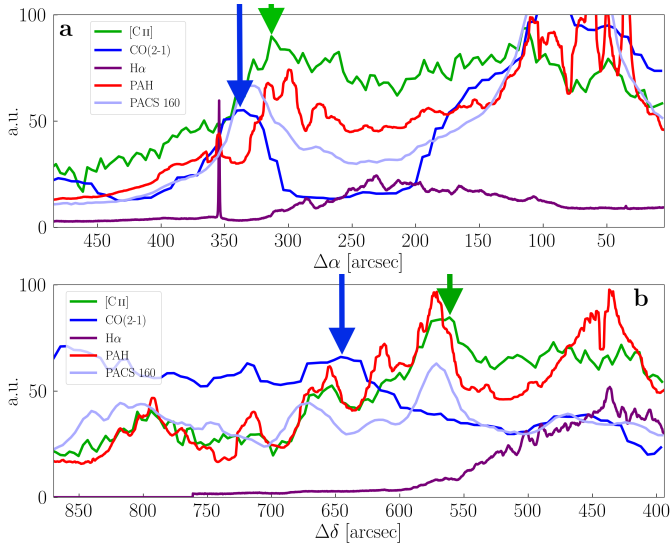


Fig. 10. Line cuts along lines a and b, indicated in Fig. 9. The arrows indicate the peaks in [C II] emission (green) and CO emission (blue) that correspond to the shell.

From our dust SEDs, we derive a mass of $M \approx 210 M_{\odot}$. However, this mass is likely contaminated by the mass of the molecular background, whose surface is visible in [C II] (cf. Fig. 8). Using only the PACS bands in the SED, reduces the mass estimate to $M \approx 110 M_{\odot}$. From the [C II] luminosity, $L_{[\text{C II}]} \approx 24 L_{\odot}$ and assuming $T_{\text{ex}} \approx 90$ K (see below), the mass is estimated to be $M \approx 55 M_{\odot}$.

We note that the limb-brightened shell of M 43 consists of two segments. The eastern shell lies closer to the central star and therefore is probably denser. We can derive the density of the shell by the distance between the [C II] and the CO peak in

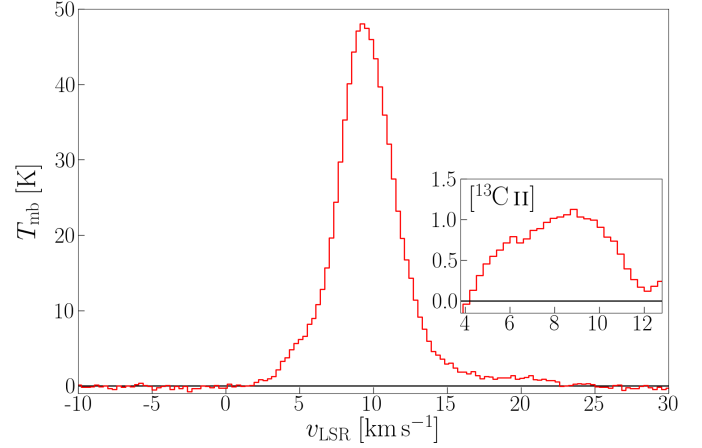


Fig. 11. Average [C II] spectrum towards the eastern shell of M 43. The inlay panel shows the residual of the spectrum, in the systemic velocity of the $^{13}\text{C II}$ $F = 2 - 1$ line, after subtracting the $^{12}\text{C II}$ fit. The $^{12}\text{C II}$ line can be fitted by a Gaussian with $T_p \approx 46.2 \pm 0.3$ K, $v_p \approx 9.6 \pm 0.1$ km s $^{-1}$, $\Delta v_{\text{FWHM}} \approx 4.6 \pm 0.1$ km s $^{-1}$; the $^{13}\text{C II}$ $F = 2 - 1$ component is fitted by a Gaussian with $T_p \approx 1.1 \pm 0.2$ K, $v_p \approx 8.6 \pm 0.3$ km s $^{-1}$, $\Delta v_{\text{FWHM}} \approx 4.8 \pm 0.8$ km s $^{-1}$. We note that a better fit of the $^{12}\text{C II}$ line can be obtained by fitting two components with $T_p \approx 30.9 \pm 1.3$ K, $v_p \approx 9.6 \pm 0.1$ km s $^{-1}$, $\Delta v_{\text{FWHM}} \approx 3.3 \pm 0.1$ km s $^{-1}$ and $T_p \approx 17.5 \pm 1.3$ K, $v_p \approx 9.8 \pm 0.1$ km s $^{-1}$, $\Delta v_{\text{FWHM}} \approx 6.8 \pm 0.2$ km s $^{-1}$, but both fits leave significant residuals.

a line cut through that region (Fig. 10a), $\Delta d \approx 20'' \approx 0.04$ pc between the [C II] peak at $\Delta \alpha \approx 310''$ and the CO peak at $\Delta \alpha \approx 330''$. Assuming a typical PDR structure with $\Delta A_V \approx 2$ between the PDR front, traced by [C II], and the CO peak, we arrive at a density of $n \approx 3 \times 10^4$ cm $^{-3}$. In the northern shell (Fig. 10b) we derive a density of $n \approx 8 \times 10^3$ cm $^{-3}$ with $\Delta d \approx 80'' \approx 0.16$ pc between the [C II] peak at $\Delta \delta \approx 560''$ and the CO peak at $\Delta \delta \approx 640''$. With the shell extent above, that is $V = \frac{2\pi}{3} ((0.3 \text{ pc})^3 - (0.25 \text{ pc})^3)$, and the latter density estimate, we compute a mass of the expanding hemisphere of $M \approx 7 M_{\odot}$, which is significantly lower than the mass derived from the dust optical depth and the [C II] luminosity. Given the potential contamination of these mass estimates by background molecular cloud material, we elected to go with the latter estimate for the gas mass.

When averaging over the eastern limb-brightened shell of M 43, we detect the $^{13}\text{C II}$ $F = 2 - 1$ line at a 4σ level, as shown in Fig. 11. From this⁵ we obtain an average $\tau_{[\text{C II}]} \approx 2.4^{+1.0}_{-1.4}$ and an excitation temperature of $T_{\text{ex}} \approx 89^{+20}_{-5}$ K. This translates into a C $^{+}$ column density of $N_{\text{C}^{+}} \approx 2.7^{+0.9}_{-1.2} \times 10^{18}$ cm $^{-2}$ along the line of sight. Assuming that most of the material is located in the limb-brightened shell, we can estimate a density in the shell with the assumed length of the line of sight of $l \sim r/2$. With $r \approx 0.3$ pc, this gives $n \approx 3 \times 10^4$ cm $^{-3}$, which is about the same as the previous estimate from the [C II]-CO peak separation. With this density we compute a gas temperature of $T_{\text{gas}} \approx 90$ K.

If we assume the [C II] emission from the limb-brightened shell to be (marginally) optical thick, we can estimate the excitation temperature from the [C II] peak temperature. This gives an average of $T_{\text{ex}} \approx 110$ K, and hence a slightly higher gas temperature than from the $^{13}\text{C II}$ estimate.

⁵ We use the peak temperature of the single-component fit, assuming that the $^{13}\text{C II}$ component corresponds to the combination of the two main components, as suggested by the similar line widths of the single-component fits.

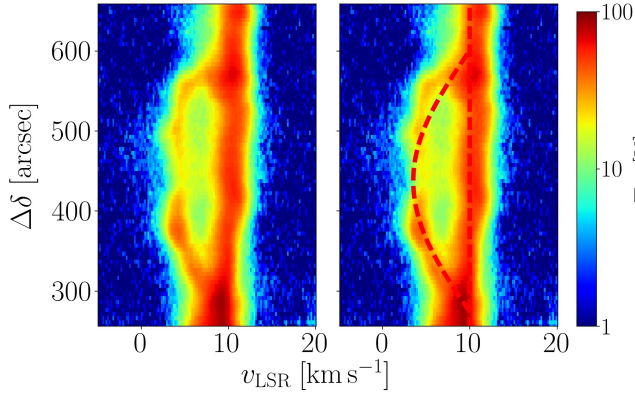


Fig. 12. [C II] pv diagram along vertical position cut 1 indicated in Fig. 2 ($\Delta\alpha = 167''\text{--}242''$), zoomed in to M43 (cf. Fig. 8). The *right panel* shows the same cut with the arc structure for an expansion velocity of 6 km s^{-1} on a background velocity of 8 km s^{-1} (red dashed lines).

Table 2. Gaussian fit parameters of spectra in Fig. 13.

$\Delta\delta$	Comp.	T_P [K]	v_P [km s $^{-1}$]	Δv_{FWHM} [km s $^{-1}$]
377''	1	43.1 ± 0.4	10.2 ± 0.1	2.9 ± 0.1
377''	2	26.4 ± 0.3	4.1 ± 0.1	2.1 ± 0.1
377''	3	10.9 ± 0.3	6.3 ± 0.2	8.0 ± 0.1
452''	1	41.6 ± 0.4	10.4 ± 0.1	2.8 ± 0.1
452''	2	10.0 ± 0.3	4.4 ± 0.1	2.0 ± 0.1
452''	3	14.9 ± 0.3	7.2 ± 0.1	8.5 ± 0.1
528''	1	44.7 ± 0.9	10.5 ± 0.1	3.3 ± 0.1
528''	2	14.9 ± 0.4	4.8 ± 0.1	1.8 ± 0.1
528''	3	14.3 ± 0.4	7.3 ± 0.2	6.9 ± 0.2

3.3.2. Expansion velocity

The [C II] pv diagram running through M43 clearly exhibits a half shell structure (Fig. 12). From the spectra taken towards this region (Fig. 12), we measure an expansion velocity of $v_{\text{exp}} \approx 6\text{ km s}^{-1}$. The bubble only expands towards us, away from the background molecular cloud. We do not see an expanding CO counterpart (cf. Fig. 8). The pv diagram is consistent with the radius of the shell of $r \approx 150'' \approx 0.3\text{ pc}$ and the expansion velocity of $v_{\text{exp}} \approx 6\text{ km s}^{-1}$, both values are much less than those derived for the Trapezium wind-blown bubble. Also, in Fig. 12, we observe [C II] emission from within the shell arc, presumably stemming from the expanding ionized gas.

The eastern shell of M43, that lies closer to the shell center, moves outward at a velocity of about $v_{\text{exp}} \approx 2.5\text{ km s}^{-1}$ (estimated from channel maps, see above and Appendix B). This corroborates the thesis that this is a denser region compared to other structures in M43. Again, the systematic uncertainty of the mass estimate is of the order of 50%, systematic uncertainties of the estimates of the extent of the shell and of the expansion velocity are about 30%.

3.4. NGC 1977

3.4.1. Geometry, mass and physical conditions

As for M42 and M43, the shell structure of NGC 1977 is almost spherical, but again it is offset from the central star(s). We

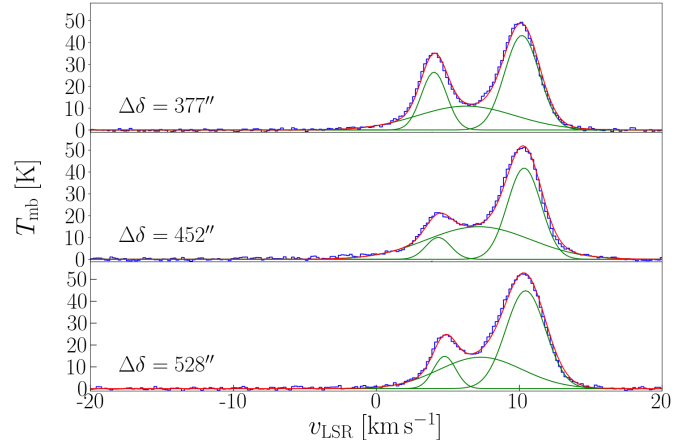


Fig. 13. [C II] spectra along position cut 1 (cf. Fig. 12) in M43 with Gaussian fits. Each spectrum is averaged over $75.5'' \times 25.2''$. The expanding shell has a distinguished emission peak. Additionally to the main component and the shell component, we fit a third, broad, component, that possibly stems from the ionized gas within the shell. Coordinate offsets indicate the lower left-hand corner of the rectangle over which the spectra are averaged; $\Delta\alpha = 242''$. The fit parameters are given in Table 2.

estimate its geometric center at $(\Delta\alpha, \Delta\delta) = (195'', 155'')$ (from 42 Orionis, $(\Delta\alpha, \Delta\delta) = (-100.4'', 1984.7'')$ from $\theta^1\text{ Ori C}$) and its outer radius with $r = 800'' = 0.22\text{ deg}$, which corresponds to $r \approx 1.6\text{ pc}$, assuming a distance of 414 pc (Menten et al. 2007). Hence, the projected distance of the bubble center from 42 Orionis is 0.5 pc . The thickness of the limb-brightened shell is $\Delta r = 7' \approx 0.8\text{ pc}$, somewhat thicker than the shell of M42, but more dilute as well. Figure 14 shows a three-color image of NGC 1977. Visible $H\alpha$ stems from the center of NGC 1977, constituting an H II region, surrounded by a shell of [C II] and constrained by a bulk CO cloud (OMC3) in the southwest.

The limb-brightened shell is seen in [C II] emission in the velocity range $v_{\text{LSR}} = 9\text{--}15\text{ km s}^{-1}$. The brightest [C II] component stems from the molecular core OMC3, which hosts a PDR at its surface towards 42 Orionis. The [C II] emission associated with this PDR is analyzed in detail by Kabanovic et al. (in prep.). With the FUV luminosity given by Kim et al. (2016), we compute an incident FUV intensity of $G_0 \approx 100$ at the shell surface.

From our τ_{160} map, we estimate the mass of the shell, where we exclude the region of OMC3. We obtain $M \approx 700 M_\odot$. With the [C II] luminosity $L_{[\text{C II}]} \approx 140 L_\odot$, we derive a mass of the [C II]-emitting gas of $M \approx 540 M_\odot$ for $T_{\text{ex}} = 50\text{ K}$, somewhat lower than the mass derived from the dust opacity, but still in good agreement⁶.

Figure 15 shows the average spectrum towards the [C II]-bright shell of NGC 1977, excluding OMC3. Here, the detection of the $^{13}\text{C II}$ $F = 2 - 1$ line is marginal with $\sigma \approx 3$. As the [C II] optical depth and excitation temperature are very sensitive to the exact $^{13}\text{C II}$ peak temperature, it is hard to derive reliable values with the uncertainties at hand (fit uncertainties and baseline ripples). With the results of a Gaussian fit as given in the caption of Fig. 15, we obtain $\tau_{[\text{C II}]} \approx 0.7 \pm 0.3$ and $T_{\text{ex}} \approx 70_{-10}^{+30}\text{ K}$. The resulting C^+ column density then is $N_{\text{C}^+} \approx 6 \pm 2 \times 10^{17}\text{ cm}^{-2}$. If we assume a column length of $r/2 \approx 0.5\text{ pc}$ in the limb-brightened shell, we estimate a density of $n \approx 2.5 \times 10^3\text{ cm}^{-3}$. This results in an estimate of the gas temperature of

⁶ The excitation temperature is not well-constrained, see analysis below.

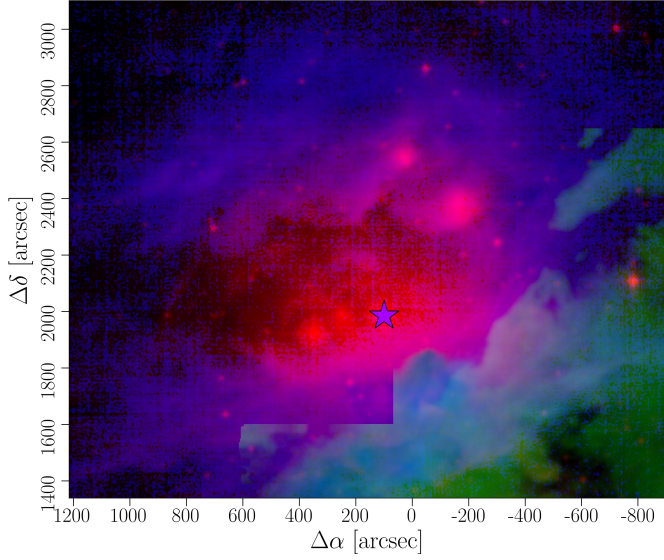


Fig. 14. Three-color image of NGC 1977. Red is $H\alpha$ emission from the ionized gas, green is line-integrated CO(2–1) emission from molecular gas (coverage only in OMC3), and blue is the [C II] line-integrated intensity, tracing the neutral gas.

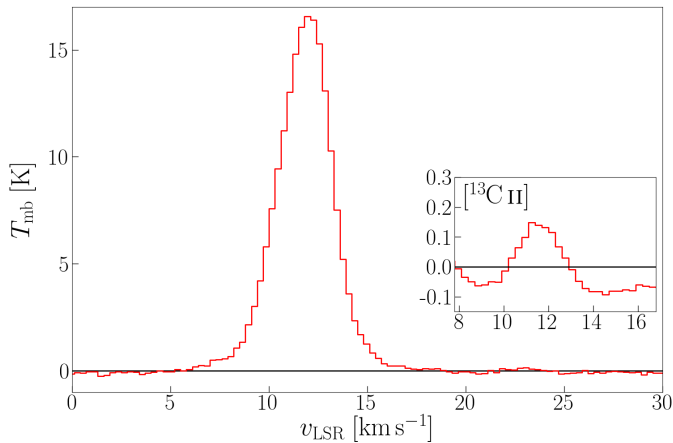


Fig. 15. Average [C II] spectrum towards [C II]-bright shell of NGC 1977 (without OMC3). The inlaid panel shows the (smoothed) residual of the spectrum, in the systemic velocity of the $[^{13}\text{C II}] F = 2 - 1$ line, after subtracting the $[^{12}\text{C II}]$ fit. The $[^{12}\text{C II}]$ component can be approximated by a Gaussian with $T_p \approx 16.5 \pm 0.1$ K, $v_p \approx 12.0 \pm 0.1$ km s $^{-1}$, $\Delta v_{\text{FWHM}} \approx 3.2 \pm 0.1$ km s $^{-1}$; the $[^{13}\text{C II}] F = 2 - 1$ component is fitted by a Gaussian with $T_p \approx 0.21 \pm 0.03$ K, $v_p \approx 11.8 \pm 0.2$ km s $^{-1}$, $\Delta v_{\text{FWHM}} \approx 2.1 \pm 0.5$ km s $^{-1}$.

$T_{\text{gas}} \approx 180$ K, which is somewhat higher than expected for the rather moderate radiation field in NGC 1977.

The mean dust optical depth from NGC 1977 (without OMC3) is $\tau_{160} \approx 2.4 \times 10^{-3}$. From this, with $r/2 \approx 0.5$ pc, we estimate a gas density of $n \approx 1 \times 10^4$ cm $^{-3}$ in the shell. With the average $T_{\text{ex}} \approx 70$ K (from the dust optical depth and the peak temperature of the [C II]), this gives $T_{\text{gas}} \approx 90$ K. From the dust optical depth and the [C II] peak temperature, we calculate $\tau_{[\text{C II}]} \sim 3$, so [C II] emission is optically thick. This is in disagreement with the result from the $[^{13}\text{C II}] F = 2 - 1$ line. However, the result obtained here seems to be more credible, as it yields a gas temperature that is more in line with a previous [C II] study of the Horsehead Nebula at similar impacting radiation field (Pabst et al. 2017). PDR models predict a surface

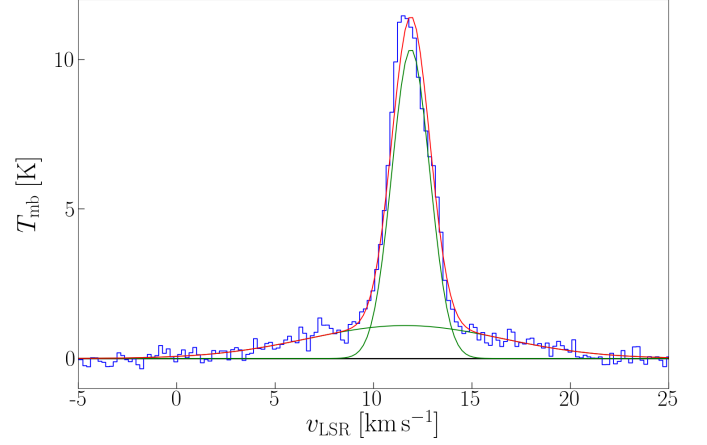


Fig. 16. [C II] spectrum towards NGC 1977, averaged over circular area with radius 125" centered at 42 Orionis ($(\Delta\alpha, \Delta\delta) = (-100.4'', 1984.7'')$), with Gaussian fits. The fit parameters are given in Table 3.

Table 3. Gaussian fit parameters of spectrum in Fig. 16.

Comp.	T_p [K]	v_p [km s $^{-1}$]	Δv_{FWHM} [km s $^{-1}$]
1	10.3 ± 0.1	11.9 ± 0.1	2.3 ± 0.1
2	1.1 ± 0.1	11.6 ± 0.2	11.6 ± 0.6

temperature of ~ 150 K (Kaufman et al. 2006; Pound & Wolfire 2008), but the [C II]-emitting layer is expected to be somewhat cooler.

In the region where the spectrum in Fig. 18 is taken, we have an average $\tau_{160} \approx 8.6 \times 10^{-4}$, corresponding to a hydrogen column density of $N_{\text{H}} \approx 5 \times 10^{21}$ cm $^{-2}$. From $H\alpha$ emission, we can estimate the electron density in the ionized gas that is contained in the shell. We obtain $n_e \approx 40$ cm $^{-3}$. Hence, with a column length of $l \sim 2$ pc the ionized gas is only a fraction of the total column density. Most of the dust emission within the column stems from the denser expanding shell. With a shell thickness of $d \approx 0.8$ pc, appropriate for the limb-brightened shell, we estimate a gas density of $n \approx 2 \times 10^3$ cm $^{-3}$. From the column density⁷ (assuming that all carbon is ionized) and the spectrum we calculate an excitation temperature of $T_{\text{ex}} \approx 37$ K and a [C II] optical depth of $\tau_{[\text{C II}]} \approx 1$. This corresponds to a gas temperature of $T_{\text{gas}} \approx 60$ K, which is somewhat lower than in the limb-brightened shell as calculated above. However, a slight overestimation of the dust optical depth of the expanding material would lead to a significantly increased estimate of the gas temperature.

Towards the center of the H II region, we observe a very broad component in the [C II] spectrum (Fig. 16). This component likely stems from the ionized gas. The expected [C II] intensity from ionized gas at a temperature of $T \sim 10^4$ K with an electron density of $n_e \approx 40$ cm $^{-3}$ and a line of sight of $l \approx 2$ pc matches the observed intensity very well. We note that the line is broader than what one would expect from thermal broadening alone. The additional broadening might be due to enhanced turbulence and the expansion movement of the gas.

⁷ We use half the column density for each of the two [C II] spectral components.

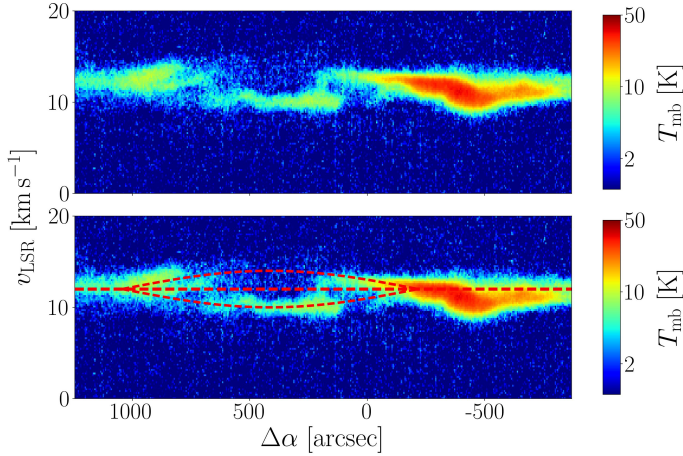


Fig. 17. [C II] pv diagram of NGC 1977 along position cut 3, indicated in Fig. 2 ($\Delta\delta = 2085'' - 2259''$). The *lower panel* shows the same cut with the arc structure for an expansion velocity of $\pm 1.5 \text{ km s}^{-1}$ (red dashed lines).

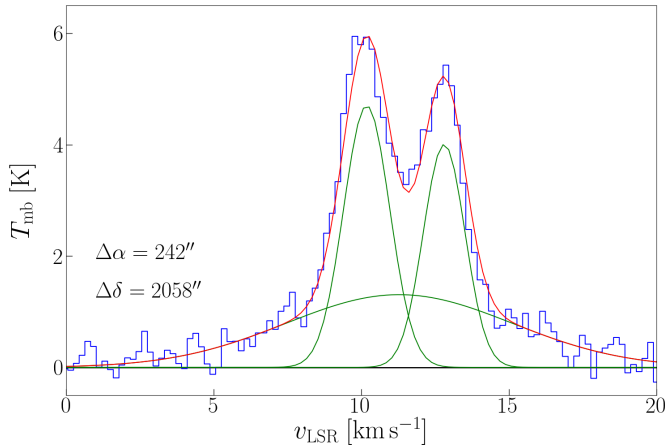


Fig. 18. [C II] spectrum along pv diagram in NGC 1977 (Fig. 17) with Gaussian fits, averaged over $201'' \times 201''$. Coordinate offsets indicate the lower left-hand corner of the square over which the spectrum is averaged. The two narrow components stem from the expanding shell, while the broad component originates in the ionized gas that is contained within the shell. Since the bubble expands in both directions, the peak-velocity difference is twice the expansion velocity, $v_{\text{exp}} \approx 1.3 \text{ km s}^{-1}$. The fit parameters are given in Table 4.

3.4.2. Expansion velocity

Figure 17 shows a [C II] pv diagram through the center of the bubble associated with NGC 1977. We recognize evidence of expansion but the arc structure is much fainter than in M 42 and M 43 and disrupted. As opposed to M 42 and M 43, there is no background molecular cloud constraining the expanding gas: we see the bubble expanding in two directions.

Since the [C II] emission from NGC 1977 is fainter than that of M 42, we have opted to determine the expansion velocity from spectra towards this region (Fig. 18), resulting in $v_{\text{exp}} \approx 1.3 \text{ km s}^{-1}$. This is consistent with the pv diagram shown in Fig. 17, from which we obtain the bubble radius $r \approx 500'' \approx 1.0 \text{ pc}$ with the expansion velocity of $v_{\text{exp}} \approx 1.5 \text{ km s}^{-1}$. As for the Veil shell and M 43, the systematic uncertainty of the mass estimate are of the order of 50%, systematic uncertainties of the estimates of the extent of the shell and of the expansion velocity are about 30%.

Table 4. Gaussian fit parameters of spectrum in Fig. 18.

Comp.	T_P [K]	v_P [km s^{-1}]	Δv_{FWHM} [km s^{-1}]
1	4.0 ± 0.2	10.2 ± 0.1	1.7 ± 0.1
2	4.7 ± 0.2	12.8 ± 0.1	1.8 ± 0.1
3	1.3 ± 0.2	11.3 ± 0.2	9.0 ± 0.7

4. Discussion

OMC1, including the Trapezium cluster, is the nearest site of active intermediate- and high-mass star formation (e.g., Hillenbrand 1997; Megeath et al. 2012, 2016; Da Rio et al. 2014; Großschedl et al. 2019 for discussions of the stellar content). Most of the stars formed and forming are low-mass stars, but also some high-mass stars, that have profound impact on the characteristics and evolution of their environment. Outside the Huygens Region, a significant massive (triple) star is the O9.5IV star θ^2 Ori A, located just to the southeast of the Orion Bar. The radiation of this star dominates the ionization structure of the gas towards the south-east of the Huygens Region (O'Dell et al. 2017). It also possesses strong winds. The most dominant star in the Orion Nebula is the O7V star θ^1 Ori C, the most massive Trapezium star. It is itself a binary, with possibly a third companion (Lehmann et al. 2010). While its exact peculiar velocity is controversial, the θ^1 Ori C is plowing away from the molecular cloud, the site of its birth, and will have travelled some 25 pc before it explodes as a supernova (O'Dell et al. 2009; Kraus et al. 2009; Pabst et al. 2019).

While the small, 0.5 pc sized Huygens Region has been extensively studied, studies on the much fainter EON are less numerous. O'Dell & Harris (2010) determine the temperature of the ionized gas within the large EON H II region to be $T \sim 8.3 \times 10^3 \text{ K}$, while electron densities decrease from $n_e \sim 3000 \text{ cm}^{-3}$ at the Trapezium stars to about $n_e \sim 30 \text{ cm}^{-3}$ 20' away, roughly as d^{-2} , with d the projected distance. Güdel et al. (2008) report that the EON exhibits significant X-ray emission, emanating from hot ($T \sim 2 \times 10^6 \text{ K}$), dilute ($n_e \sim 0.1 - 0.5 \text{ cm}^{-3}$) gas. While, in principle, ionization followed by thermal expansion of the H II region can create a bubble of $\sim 2 \text{ pc}$ size, the hot gas is the tell-tale signature that the stellar wind of massive stars, rather than stellar radiation, is driving the expansion and forming the EON cavity. As Güdel et al. (2008) note, the emission characteristics in conjunction with its structure and young age render it unlikely that the bubble is a supernova remnant. While the observed morphology is in qualitative agreement with simple models for stellar winds from massive stars (Weaver et al. 1977), the observed plasma temperature is lower than expected from refined models and suggests that mass loading of the hot plasma has been important (Arthur 2012).

Recently, the inner shocked wind bubble surrounding θ^1 Ori C has been identified in optical line observations (Abel et al. 2019). This inner shock will heat the gas in the EON that drives the expansion of a larger, outer, shell. These same observations, however, suggest that the thus heated gas is only free to escape through the south-west of the Huygens Region.

The limb-brightened edge of the Veil shell, the dense shell associated with M 42, is readily observed edge-on. It is a closed, surprisingly spherically symmetric structure enveloping the inner Huygens Region and the EON (Pabst et al. 2019), and confining the hot X-ray emitting and ionized gas observed by Güdel et al. (2008) and O'Dell & Harris (2010) in the

Table 5. Physical conditions of respective H II region and adjacent limb-brightened PDR shell in M 42, M 43, and NGC 1977.

Region		n [cm ⁻³]	T_{gas} [K]	$p_{\text{thermal}}/k_{\text{B}}$ [cm ⁻³ K]	G_0
Orion Bar	H II	5×10^3	8×10^3	8×10^7	
	PDR	6×10^5	500	3×10^8	2×10^4
Veil shell	Plasma	0.3	2×10^6	1×10^6	
	H II	50	8×10^3	8×10^5	
M 43	PDR	10^3 – 10^4	~100	1 – 10×10^5	~100
	H II	500	7.5×10^3	8×10^6	
NGC 1977	PDR	10^4	100	1×10^6	~ 2×10^3
	H II	40	~ 10^4	~ 8×10^5	
	PDR	10^3	90	9×10^4	~100

Notes. The plasma in M 42 was analyzed by Güdel et al. (2008). Data on the M 42 H II region are from O’Dell & Harris (2010), data on the M 43 H II region are from Simón-Díaz et al. (2011). We note that the density of the M 42 H II region given here is appropriate for the southern EON, as is G_0 in the Veil shell PDR.

Table 6. Comparison of pressure terms in PDRs of the Orion Bar, Veil shell, M 43, and NGC 1977.

p/k_{B}	Orion Bar	Veil shell	M 43	NGC 1977
Thermal	3×10^8	1 – 10×10^5	1×10^6	9×10^5
Magnetic	3×10^7	2×10^6	–	–
Turbulence	3×10^7	0.5 – 3×10^6	8×10^5	8×10^4
Radiation	1×10^7	1×10^5	3×10^6	8×10^4

Notes. In the Veil shell, higher pressures correspond to the limb-brightened edges, while lower pressures apply to the foreground expanding shell. The radiation pressure is computed from the total luminosity of the central star.

foreground. Likewise, the H II regions of M 43 and NGC 1977 are surrounded by rather dense shells. The limb-brightened shell of M 43 exhibits a PDR-like layered structure (cf. Fig. 10). At the southern edge of the shell surrounding NGC 1977 one encounters OMC3, which also possesses a PDR-like structure, irradiated by 42 Orionis (Kabanovic et al., in prep.).

For our analysis we adopt a distance of 414 ± 7 pc (Menten et al. 2007) towards the Orion Nebula complex, although more recent results suggest somewhat lower values, 388 ± 5 pc (Kounkel et al. 2017), which is in agreement with *Gaia* DR2 results (Großschedl et al. 2018). In view of other uncertainties in the analysis, we consider this a minor source of uncertainty.

4.1. The pressure balance

Table 5 summarizes the physical conditions in the H II regions and the limb-brightened PDR shells in M 42, M 43, and NGC 1977. Table 6 summarizes the various pressure terms in the total pressure $p_{\text{tot}} = p_{\text{thermal}} + p_{\text{magnetic}} + p_{\text{turb}} + p_{\text{lines}} + p_{\text{rad}}$ in the PDRs of M 42 (Orion Bar and Veil shell), M 43, and NGC 1977.

The thermal pressure, $p_{\text{thermal}} = nkT$, in the Orion Bar is controversial. Constant-pressure and H II region models of atomic and molecular lines of Pellegrini et al. (2009) and observations of molecular hydrogen by Allers et al. (2005) ($n \approx 10^5$ cm⁻³, $T_{\text{gas}} \approx 500$ K) indicate a pressure of $p/k_{\text{B}} \approx 5 \times 10^7$ K cm⁻³. Observations of [C II] and [O I] emission in the Orion Bar suggest similar values ($n \gtrsim 10^5$ cm⁻³, $T_{\text{gas}} \gtrsim 300$ K) (Bernard-Salas et al. 2012; Goicoechea et al. 2015). High-J CO observations indicate a higher gas pressure within the Bar, 3×10^8 K cm⁻³

(Joblin et al. 2018). This latter value is in agreement with observations of carbon radio recombination lines (CRRLs) that measure the electron density in the PDR directly ($n \gtrsim 4$ – 7×10^5 cm⁻³) (Cuadrado et al. 2019). The thermal pressures in the EON portion of M 42, M 43, and NGC 1977 have been calculated from the parameters given in Table 5.

The magnetic field strength in the Orion Bar has been estimated from the far-IR dust polarization using the Davis-Chandrasekhar-Fermi method to be $300 \mu\text{G}$ (Chuss et al. 2019). This corresponds to a magnetic field pressure, $p_{\text{magnetic}} = B^2/8\pi$, of 3×10^7 K cm⁻³. The magnetic field in the Veil in front of the Huygens Region is measured to be $B_{\text{los}} \approx -50$ – $(-75) \mu\text{G}$ from the H I and OH Zeeman effect (Troland et al. 2016); we compute the magnetic field pressure from the lower value⁸. The turbulent pressure, $p_{\text{turb}} = \rho\sigma_{\text{turb}}^2$, is calculated from the [C II] line width in the average spectra towards the Veil shell, M 43, and NGC 1977 (Figs. 3, 11, and 18) after correction for thermal broadening at a kinetic temperature of $T_{\text{gas}} \sim 100$ K (cf. Table 5); with a typical line width of $\Delta v_{\text{FWHM}} \approx 4$ km s⁻¹ this gives $\sigma_{\text{turb}} \approx 1.7$ km s⁻¹. In the Orion Bar, we use $\sigma_{\text{turb}} \approx 1.5$ km s⁻¹ (Goicoechea et al. 2015).

The radiation pressure is in principle given by $p_{\text{rad}} = L_{\star}/(4\pi R_{\text{S}}^2 c)$; the luminosities of the central stars are given in Table 8. We assume the (projected) distances $R_{\text{S}} \approx 4$ pc for the (southern) Veil shell, $R_{\text{S}} \approx 0.25$ pc for M 43, and $R_{\text{S}} \approx 1.0$ pc for NGC 1977. However, for the Orion Bar, a direct measurement of the infrared flux suggests a value that is an order of magnitude lower than the pressure calculated from the stellar luminosity and the projected distance of $R_{\text{S}} \approx 0.114$ pc (Pellegrini et al. 2009), an incident radiation field of $G_0 = 2.6 \times 10^4$ (Marconi et al. 1998; Salgado et al. 2016). Hence, we choose to calculate the radiation pressure in the Orion Bar from this latter value. We note that in the other cases the radiation pressure given in Table 6 is, thus, an upper limit.

Resonant scattering of Ly α photons constitutes the major contribution to the line pressure term p_{lines} . We expect this term to be at most of the order of the radiation pressure and hence negligible in the cases presented here (Krumholz & Matzner 2009).

We consider now the PDR associated with the Orion Bar, which is likely characteristic for the dense PDR associated with the OMC1 core. Perusing Tables 5 and 6, we conclude that the thermal pressure derived from high-J CO lines and CRRLs

⁸ The magnetic pressure is computed from $B_{\text{tot}} = 3B_{\text{los}}^2$.

exceeds the turbulent and magnetic pressure by an order of magnitude. While the [C II] line stems from the surface of the PDR, high-J CO lines and CRRLs stem from deeper within the PDR. Models of photoevaporating PDRs suggest that the pressure increases with depth into the PDR (Bron et al. 2018). The [C II]-emitting PDR surface may be well described by a lower pressure ($5 \times 10^7 \text{ K cm}^{-3}$), in which case approximate equipartition holds between the three pressure terms. Their combined pressures of $1 \times 10^8 \text{ K cm}^{-3}$ then is balanced by the thermal pressure of the ionized gas, $8 \times 10^7 \text{ K cm}^{-3}$, with a contribution from the radiation pressure.

For the PDR in the Veil shell, the thermal, turbulent and magnetic pressure are again in approximate equipartition. In this case, there is approximate pressure equilibrium between the combined pressures in the PDR gas and the combined pressures of the ionized gas and the hot plasma in the EON. Overall, there is a clear pressure gradient from the dense molecular cloud core behind the Trapezium stars to the Veil shell in front. This strong pressure gradient is responsible for the rapid expansion of the stellar wind bubble towards us and sets up the ionized gas flow, which (almost freely) expands away from the ionization front at about 10 km s^{-1} (García-Díaz et al. 2008; O’Dell et al. 2009). During the initial phase, the thermal pressure of the hot gas drives the expansion of the shell and radiation pressure provides only a minor contribution (Silich & Tenorio-Tagle 2013). Radiation pressure takes over once the plasma has cooled through energy conduction and the bubble enters the momentum-driven phase.

Turning now towards the H II regions, M 43 and NGC 1977, we note that the sum of the thermal and turbulent pressures in the PDRs of these two regions is well below the thermal pressure of the ionized gas. While, in principle, the pressure could be balanced by the magnetic field, we expect equipartition to hold as well. Rather, we take this pressure difference to imply that the overpressure of the ionized gas drives the expansion of these H II regions. We note that radiation pressure is not important for these two nebulae.

4.2. Rayleigh-Taylor instability of the Veil shell

Molecular clouds, under the influence of massive stars, can develop hydrodynamical instabilities that compress or fragment the cloud. In our [C II] data as well as in the H α image, we see evidence that the expanding gas might suffer from Rayleigh-Taylor instability, leading to the formation of elongated structures perpendicular to the expanding surface (cf. Figs. 1a and b). These fingers are particularly clear in the EON towards the south of the Veil shell. Figure 19 shows this part of the Veil shell with its complex velocity structure. Rayleigh-Taylor instability occurs at the interface of a “heavy” fluid (here the expanding neutral [C II] gas) floating on top of a “light” fluid (here the hot plasma). This instability leads to increased turbulence and mixing of the gas. The presence of magnetic fields may alter the growth behavior of the characteristic structures, but it is yet under debate whether Rayleigh-Taylor instability will be enhanced or suppressed (Stone & Gardiner 2007; Carlyle & Hillier 2017), the details likely depending crucially on the magnetic field configuration, which is hard to determine observationally.

The scale size of the unstable region after a time t is given by:

$$h = \alpha A g t^2, \quad (10)$$

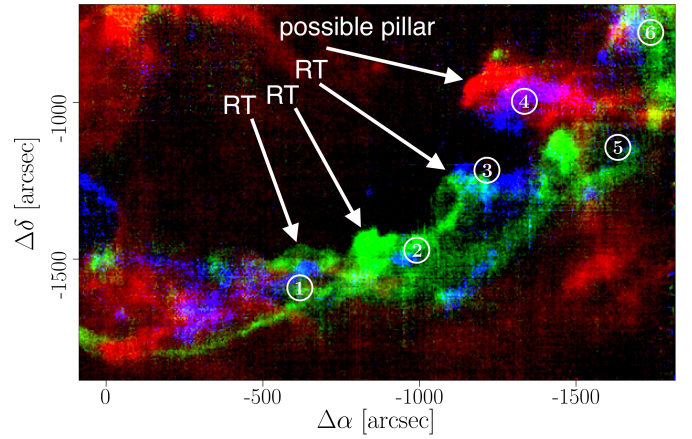


Fig. 19. Three-color image of [C II] velocity channels of the southern Veil shell. Blue is the velocity channel $v_{\text{LSR}} = 0\text{--}2 \text{ km s}^{-1}$, green $v_{\text{LSR}} = 4\text{--}6 \text{ km s}^{-1}$, and red $v_{\text{LSR}} = 8\text{--}10 \text{ km s}^{-1}$. Arrows indicate structures that resemble fingers formed due to the Rayleigh-Taylor (RT) instability. One of these, labeled “possible pillar”, might also be formed by an overdensity encountered by the expanding shell and subsequently sculpted by the strong stellar radiation field, as it also is observed in CO (cf. Fig. 1c). The spectra shown in Fig. 20 were extracted towards the areas indicated by the numbered circles.

where g is the (constant) acceleration and the Atwood number $A = \frac{n_1 - n_2}{n_1 + n_2}$ is a measure of the density contrast across the contact discontinuity (Chevalier et al. 1992; Duffell 2016). In this case, $A \sim 1$, as the density contrast is large. The parameter α is determined by experiments and numerical simulations to be ~ 0.05 . Realizing that the radius of the contact discontinuity is $R_{\text{cd}} = \frac{1}{2} g t^2$, experiments and simulations predict that $h/R_{\text{cd}} \sim 0.1$, which is in good agreement with the observed structures, that have a typical height of $\sim 100'' \approx 0.2 \text{ pc}$ in a shell with a radius of $\sim 2.5 \text{ pc}$. This lends further support for the interpretation of the observed morphology as the result of the Rayleigh-Taylor instability and for the general interpretation of the dominance of the stellar wind in driving the expansion of the shell.

[C II] observations provide a unique opportunity to probe the injection of turbulence into a molecular cloud through expanding shock waves, as [C II] emission traces the surface layer that transmits the shock wave into the surrounding medium. The morphology and velocity structure of our [C II] observations seem to indicate the importance of Rayleigh-Taylor and Kelvin-Helmholtz instabilities⁹ in the transmittance of turbulence into the expanding Veil shell. The simulations of Nakamura et al. (2006) show a similar velocity structure in the synthesized spectra as our observed spectra (Fig. 20). With a typical velocity dispersion of 3 km s^{-1} , the energy injected into the Veil shell by the Rayleigh-Taylor instability can be estimated at $3^2/13^2$ of the kinetic energy of the Veil shell, that is $1.4 \times 10^{47} \text{ erg}$. Such macro-turbulence, associated with cloud destruction, will eventually be converted into micro-turbulence of the cloud medium (Nakamura et al. 2006). Post-processing of such numerical simulations in the [C II] emission and comparison to the data might be very illuminating.

⁹ Kelvin-Helmholtz instability in the Orion Nebula has been studied by Berné et al. (2010); Berné & Matsumoto (2012). The characteristic “ripples” they detect in the western shell in PAH and CO emission are also present in the [C II] emission from that region.

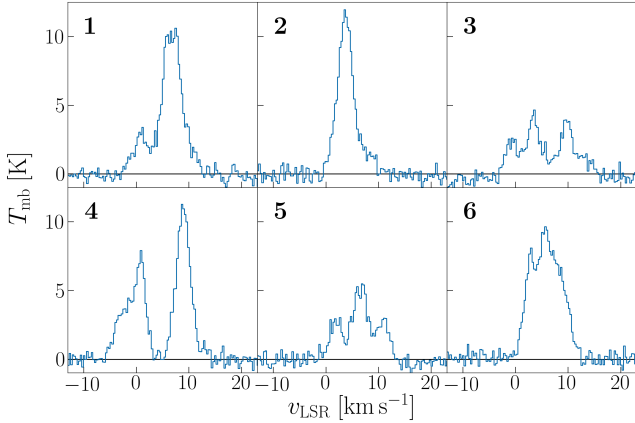


Fig. 20. [C II] spectra towards southern Veil shell. Each spectrum is averaged over a circle with a radius of $40''$ as indicated in Fig. 19. We note that each spectrum consists of multiple line components, which is characteristic of thermodynamic instabilities.

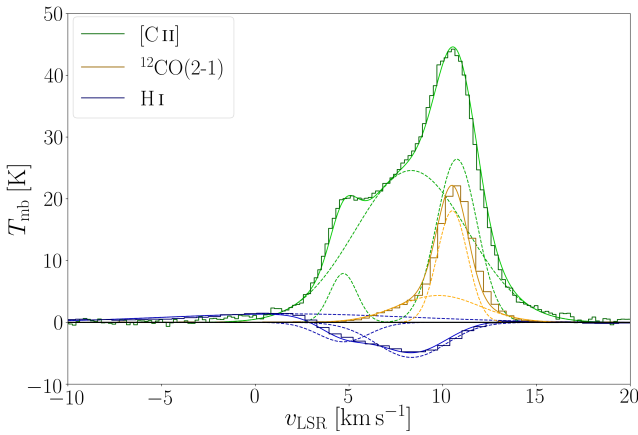


Fig. 21. [C II] (green), $^{12}\text{CO}(2-1)$ (yellow), and H I (blue) spectra towards the center of M 43, averaged over a circle with radius $r \simeq 40''$ and center $(\Delta\alpha, \Delta\delta) = (-226'', 440'')$. Plotted are also the results of Gaussian fits (dashed lines). The fit parameters are given in Table 7. The H I spectrum is multiplied by 10^{-2} to fit the scale.

4.3. The structure of M 43

Both [C II] and H I show three velocity components while CO shows only two (Fig. 21 and Table 7). We attribute the [C II] high-velocity component (10.7 km s^{-1}) to emission from the background molecular gas associated with OMC1, that we also recognize in CO emission (cf. Fig. 8). The 4.7 km s^{-1} [C II] component can be attributed to a half-shell expanding towards us. As this component is also visible in H I absorption against the radio continuum emission from the H II region, this component can be placed firmly in front. We note the difference in line width between the H I and [C II] (3.2 km s^{-1} versus 1.7 km s^{-1}), which we attribute to the importance of thermal broadening for the former. This would imply a temperature of the neutral gas of $\sim 150 \text{ K}$.

The 8.3 km s^{-1} [C II] component is more enigmatic. Given its large line width, we are tempted to associate this component with emission from the ionized gas. However, a 8.3 km s^{-1} component is also present in absorption in H I and this would place it in front of the ionized gas. Perhaps, this H I component is really associated with the Veil partially overhanging M 43, whereas the [C II] component is clearly confined to the interior of M 43 (cf. Fig. 12).

Table 7. Gaussian fit parameters of spectra in Fig. 21.

Line	Comp.	T_p [K]	v_p [km s^{-1}]	Δv_{FWHM} [km s^{-1}]
[C II]	1	26.4 ± 0.3	10.7 ± 0.1	2.6 ± 0.1
[C II]	2	24.6 ± 0.2	8.3 ± 0.1	7.0 ± 0.1
[C II]	3	7.9 ± 0.3	4.7 ± 0.1	1.7 ± 0.1
$^{12}\text{CO}(2-1)$	1	18.1 ± 0.1	10.5 ± 0.1	1.9 ± 0.1
$^{12}\text{CO}(2-1)$	2	4.4 ± 0.1	9.8 ± 0.1	5.2 ± 0.1
H I	1	-5.7 ± 0.2	8.3 ± 0.2	4.4 ± 0.3
H I	2	-3.1 ± 0.3	4.7 ± 0.2	3.2 ± 0.3
H I	3	1.4 ± 0.2	1.7 ± 0.6	15.5 ± 0.9

Notes. The H I peak temperatures have to be multiplied by 10^2 to obtain the main-beam temperature.

Furthermore, we do not see a counterpart to the CO 9.8 km s^{-1} component in [C II] and this gas must be associated with a structure in OMC1. Finally, the very broad, low velocity (1.7 km s^{-1}) H I emission component seems to form a coherent structure with H I emission associated with the Northeast Dark Lane (as can be seen from the comparison of the pv diagrams in Fig. 8). This H I component is also seen in dust extinction but there is no counterpart in the [C II] line, in the dust continuum at $70 \mu\text{m}$, or in the PAH emission at $8 \mu\text{m}$. Hence, this component is not illuminated by either θ^1 Ori C or NU Ori, placing this material firmly in front of the Veil. As has been suggested by Troland et al. (2016), this molecular gas very likely has been undisturbed by the star-formation process in OMC1.

In the [C II] line-integrated map (cf. Fig. 9), the limb-brightened shell structure of M 43 separates into two parts, with a break towards the east. This rupture is reflected in the pv diagram (Fig. 12) through the center of M 43, exhibiting a gap in the middle of the arc. In pv diagrams along the RA axis, this disruption, however, is located in the western part of M 43 (cf. Fig. C.1)

4.4. The Veil stellar-wind bubble

Güdel et al. (2008) in their influential paper on the X-ray emission from Orion revealed that the interior of the Veil shell as outlined by the [C II] line, the $8 \mu\text{m}$ PAH emission, and the $70 \mu\text{m}$ dust emission is filled with a hot ($T \sim 2 \times 10^6 \text{ K}$), tenuous ($n \sim 0.5 \text{ cm}^{-3}$) plasma with a total mass of $\sim 0.07 M_\odot$. This hot plasma is generated by the reverse shock acting on the fast stellar wind originating from θ^1 Ori C. The observations reported in this study provide the velocity, radius and mass of the shell swept up by the bubble. Following Güdel et al. (2008), we will use the stellar wind theory of Castor et al. (1975) and Weaver et al. (1977) to analyze these data.

Based on models of Castor et al. (1975) we have obtained the following two time-dependent equations for a thin shell expanding under the influence of stellar winds, under the assumption that the stellar wind is constant; this assumption is valid during most of the lifetime of a star (Haid et al. 2018) and also in the so-called snowplow phase that is discussed by Castor et al. (1975):

$$R_S(t) \simeq 28 \left(\frac{\dot{M}_6 v_{2000}^2}{n_0} \right)^{1/5} \left(\frac{t}{1 \text{ Myr}} \right)^{3/5} \text{ pc}, \quad (11)$$

$$\dot{R}_S(t) \simeq 16.4 \left(\frac{\dot{M}_6 v_{2000}^2}{n_0} \right)^{1/5} \left(\frac{t}{1 \text{ Myr}} \right)^{-2/5} \text{ km s}^{-1}, \quad (12)$$

where \dot{M}_6 is the mass-loss rate in $10^{-6} M_\odot \text{ yr}^{-1}$, v_{2000} is the wind velocity in 2000 km s^{-1} , and n_0 is the density of the ambient, uncompressed gas. For θ^1 Ori C, the wind parameters we adopt are $\dot{M}_6 \simeq 0.4$ and $v_{2000} \simeq 1.25$ (Howarth & Prinja 1989; Stahl et al. 1996).

We thus have two equations (R_S, \dot{R}_S) and two unknowns (n_0, t). We denote the solution we find for the time between the onset of expansion and the present time by t_0 . Re-arranging Eqs. (11) and (12) gives

$$t_0 \simeq 0.06 \left(\frac{R_S}{1 \text{ pc}} \right) \left(\frac{10 \text{ km s}^{-1}}{\dot{R}_S} \right) \text{ Myr}, \quad (13)$$

$$n_0 \simeq 3.5 \times 10^3 (\dot{M}_6 v_{2000}^2) \left(\frac{1 \text{ pc}}{R_S} \right)^2 \left(\frac{10 \text{ km s}^{-1}}{\dot{R}_S} \right)^3 \text{ cm}^{-3}. \quad (14)$$

From our observations we estimate the present-day values $R_S(t_0) \simeq 4 \pm 0.5 \text{ pc}$ and $v_{\text{exp}} = \dot{R}_S(t_0) \simeq 13 \pm 2 \text{ km s}^{-1}$ at the far (south) side of the expanding shell. With these values, we obtain for the unknowns $n_0 \simeq 5 \pm 2 \times 10^1 \text{ cm}^{-3}$ and $t_0 \simeq 0.2 \pm 0.05 \text{ Myr}$.

With these values, the temperature of the hot plasma inside the bubble and its density are predicted by the model to be $T_{\text{plasma}} \simeq 2.3 \pm 0.2 \times 10^6 \text{ K}$ and $n_{\text{plasma}} \simeq 0.2 \pm 0.05 \text{ cm}^{-3}$ (Castor et al. 1975). This is in excellent agreement with the X-ray observations by Güdel et al. (2008). However, numerical models of Arthur (2012), that take into account saturation of thermal conduction at the shell interface and mass loading by proplyds in the Orion nebula, produce hotter gas with $T_{\text{plasma}} \sim 10^7 \text{ K}$. Yet, the mixing efficiency of the photo-evaporation flow from the proplyds with the stellar wind material is not well constrained and a major source of uncertainties.

In an alternative approach, we fit the five observables ($R_S, v_S, \dot{M}_S, T_{\text{plasma}}, n_{\text{plasma}}$) = (2.7 pc, 13 km s^{-1} , $1500 M_\odot$, $2 \times 10^6 \text{ K}$, 0.3 cm^{-3}) with the two parameters t_0 and n_0 , given the expressions by Castor et al. (1975). From a weighted least-square fit, with relative errors (0.2, 0.2, 0.5, 0.3, 0.5), we find the best fit for $t_0 \simeq 0.24 \pm 0.05 \text{ Myr}$ and $n_0 \simeq 1.7 \pm 0.7 \times 10^2 \text{ cm}^{-3}$. In this fit, only the last three observables are fitted in good agreement; in contrast, the shell radius is predicted to be 3.8 pc and the expansion velocity as 9 km s^{-1} . The plasma temperature and density do not depend strongly on t_0 and n_0 (Castor et al. 1975). Adopting a lower gas mass of $600 M_\odot$ results in a better fit with $t_0 \simeq 0.17 \pm 0.05 \text{ Myr}$ and $n_0 \simeq 1.0 \pm 0.6 \times 10^2 \text{ cm}^{-3}$. In this scheme, however, we rely on the spherical symmetry of the problem, which is not applicable for the Orion Nebula expanding predominantly along its steepest density gradient. Considering expansion in an ambient medium with a density gradient scaling with R_S^{-2} alters the time-dependent behavior of the bubble kinematics considerably (Ostriker & McKee 1988, Sect. VII).

From the morphology of the expansion in the eastern arm of the shell (cf. Appendix B, Figs. B.1 and B.2), we obtain with $R_S(t) \simeq 1.75 \text{ pc}$ and $\dot{R}_S(t) \simeq 4.25 \text{ km s}^{-1}$ $n_0 \simeq 8 \times 10^3 \text{ cm}^{-3}$ and $t_0 \simeq 0.25 \text{ Myr}$. Here, the ambient gas density is thus much higher.

The derived lifetime of the bubble, $t_0 \simeq 0.2 \text{ Myr}$, indicates that the onset of the gas coupling to the stellar wind is rather recent, but agrees with the presumed ages of the Trapezium cluster and θ^1 Ori C, which is $< 1 \text{ Myr}$ with a median age of the stellar population of 0.3 Myr (Prosser et al. 1994; Hillenbrand 1997). In contrast, Simón-Díaz et al. (2006) give an age of θ^1 Ori C of $2.5 \pm 0.5 \text{ Myr}$, derived from optical spectroscopy of the stars in the Trapezium cluster, which is much longer than the expansion time scale of the Veil bubble. We note, though, that the star has to leave the dense core where it was born before large-scale

expansion can set on in a relatively dilute ambient medium. We expect this time to be of the order of 0.1 Myr , considering the peculiar velocity of θ^1 Ori C (Vitrichenko 2002; Stahl et al. 2008; O'Dell et al. 2009). From the absence of evidence for the destruction of nearby proplyds and interaction between the moving foreground layers, O'Dell et al. (2009) estimate the time scale since θ^1 Ori C has moved into lower-density material, starting to ionize the EON, is of a few 10^4 yr . This estimate is an order of magnitude younger than the expansion time we find. However, from modelling the disk masses of proplyds close to θ^1 Ori C, Störzer & Hollenbach (1999) find that θ^1 Ori C can be significantly older than 10^5 yr if the orbits of the proplyds are radial. Salgado et al. (2016) derive an age of 10^5 yr for θ^1 Ori C from the mass of the Orion Bar.

For the density within the shell, the compressed gas, the simple model of Castor et al. (1975) gives

$$n_s = \frac{\mu \dot{R}_S^2}{k T_s} n_0. \quad (15)$$

If the temperature in the shell is $T_s = 80 \text{ K}$, as assumed by Castor et al. (1975), and $\mu/m_H = 1.3$, assuming atomic H I gas, the density within the shell becomes $n_s \simeq 200 (\dot{R}_S / 10 \text{ km s}^{-1})^2 n_0$. In the southern shell, this then yields $n_s \simeq 400 n_0 \simeq 2 \times 10^4 \text{ cm}^{-3}$. In the eastern bright arm of the shell, we expect a shell density of $n_s \simeq 50 n_0 \simeq 5 \times 10^5 \text{ cm}^{-3}$: here, the density is much higher but also the shell is much thinner than in the southern part. Both theoretical densities are an order of magnitude higher than what we estimated from observations.

With a mass of the expanding gas shell of $M \simeq 1500 M_\odot$ and an expansion velocity of $v_{\text{exp}} \simeq 13 \text{ km s}^{-1}$, the kinetic energy in the shell is computed to be $E_{\text{kin}} \simeq 2.5 \times 10^{48} \text{ erg}$. Dividing this energy by the expansion time scale provides us with a measure that we can compare to the wind luminosity of the presumed driving star θ^1 Ori C. This yields $\frac{E_{\text{kin}}}{t_0} \simeq 4 \times 10^{35} \text{ erg s}^{-1}$. Comparing this number with the wind luminosity, $L_w \simeq 8 \times 10^{35} \text{ erg s}^{-1}$, we estimate a wind efficiency of about 50%. Adding the wind of θ^2 Ori A, which is comparable to the stellar wind of θ^1 Ori C, with $L_w \simeq 2 \times 10^{35} \text{ erg s}^{-1}$, reduces the wind efficiency to 40%; the stellar wind parameters of θ^2 Ori A are $\dot{M}_6 \sim 0.08$ and $v_{2000} \sim 1.45$ (Petit et al. 2012). Adding both winds in the above analysis, would increase densities by a factor 1.3, but has no effect on the expansion time.

During the initial stages, the swept up shell will be very thin and the stellar ionizing flux will be able to fully ionize the shell. Once the shell has swept up enough material, the ionization front will become trapped in the shell. The Veil shell has already reached this later stage as evidenced by the morphology of the shell in H α and [C II] emission (cf. Fig. 1) and the narrow line width of the [C II] line. In addition, we note that bright PAH emission (cf. Fig. 1 in Pabst et al. 2019) mostly originates from the neutral gas in PDRs and is very weak if associated at all with ionized gas. For the ambient densities we estimated above, that is $n_0 \simeq 2\text{--}5 \times 10^1 \text{ cm}^{-3}$, the time when the shell becomes neutral is $t \simeq 0.1\text{--}0.2 \text{ Myr}$ according to the Weaver et al. (1977) model¹⁰. This is in good agreement with our estimate of the expansion time.

As the [C II] observations reveal, the strong density gradient towards the front of the cloud has produced a rapid expansion of the bubble towards us. We note that the 13 km s^{-1} expansion velocity exceeds the escape velocity from OMC1 (2 km s^{-1}) and

¹⁰ If the density is actually higher, the ionizing radiation gets trapped earlier.

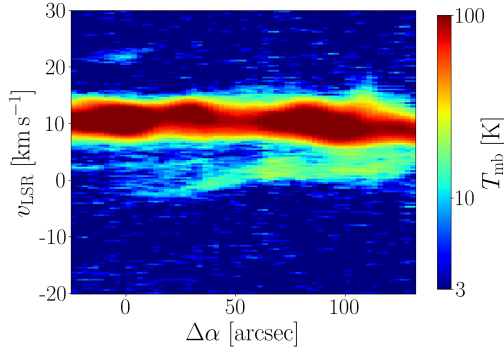


Fig. 22. PV diagram along position cut shown in Fig. 13 of Van der Werf et al. (2013), perpendicular to the Orion Bar through the Huygens Region.

eventually the swept-up mass will be lost to the environment. In addition, the bubble will break open, releasing the hot plasma and the expanding ionized gas. Inspection of the pv diagrams (Figs. C.1 and C.2) indicates that the Veil shell is quite thin in some directions and break out may be “imminent”. Eventually, the shell material, the hot plasma, and the entrained ionized gas will be mixed into the interior of the Orion-Eridanus superbubble. The next supernova that will go off, one of the Orion Belt stars in ~ 1 Myr, will sweep up this “loose” material and transport it to the walls of the superbubble. The last time this happened, about 1 Myr ago, this created Barnard’s loop.

New numerical simulations show that the effects of stellar wind on their surroundings depends strongly on the characteristics of the medium (Haid et al. 2018). Stellar winds dominate if the bubble expands into an ambient warm ionized medium (WIM, $T \sim 10^4$ K, $n \sim 0.1$ cm $^{-3}$). If the ambient medium is colder and neutral (CNM, $T \sim 100$ K, $n \sim 100$ cm $^{-3}$), ionizing radiation is the dominant driving force. The warm neutral medium (WNM, $T \sim 2 \times 10^3$ K, $n \sim 1$ cm $^{-3}$) is an intermediate case. However, these models are not descriptive of the situation of θ^1 Ori C. New studies need to investigate the effects of stellar winds of a star in the outskirts of a molecular cloud, an environment that is rather dilute ($n \sim 10$ cm $^{-3}$) and subject to density gradients. We realize that the Veil shell provides an excellent test case for models of stellar wind expansion into a surrounding medium given the large number of observational constraints, including the mass of the shell, the temperature and density of the shell and of the plasma, the velocities of the shell and the dense ionized gas in the Huygens Region.

4.5. The expanding bubble of θ^2 Ori A

Van der Werf et al. (2013) discuss the shell structure that seems to surround θ^2 Ori A, their component L, that can be identified in our [C II] data, as well. Figure 22 shows the same cut for the [C II] intensity as Fig. 13 of Van der Werf et al. (2013) for the H I optical depth. Component L is a rather small arc-like structure, $r \approx 50'' \approx 0.1$ pc extending to a LSR velocity of $v_{\text{LSR}} \approx -3.2$ km s $^{-1}$. This would translate into an expansion velocity of $v_{\text{exp}} \approx 11$ km s $^{-1}$. If this was a wind blown bubble, we would obtain from Eqs. (13) and (14), $t_0 \approx 0.006$ Myr and $n_0 \approx 4 \times 10^4$ cm $^{-3}$. This might be reasonable, considering that the star might only very recently have emerged from the dense material were it was born. It might also be that θ^2 Ori A is the ionizing source for this structure, but not its cause. Schulz et al. (2006) estimate the stellar age to be ~ 0.3 Myr, similar to θ^1 Ori C, but not much younger.

Also the arc-like structure D of Van der Werf et al. (2013) has been discussed as associated with θ^2 Ori A (García-Díaz & Henney 2007), but Van der Werf et al. (2013) attribute it to θ^2 Ori B, an early B-type star. However, in the H I cuts component D only appears with a radius of $r \approx 100''$, while we observe a larger structure, $r \approx 500'' \approx 1$ pc, that has a large negative velocity ($v_{\text{LSR}} \approx -20$ km s $^{-1}$). The latter’s geometric center seems to lie more to the southeast, as can be seen in our pv diagrams (cf. Fig. C.1). We do not observe component D in Fig. 22, indicating that it is not illuminated by UV radiation and hence a foreground component. Assuming the larger [C II] structure to be the wind-blown bubble of θ^2 Ori A, comparison with models would give $t_0 \approx 0.002$ Myr and $n_0 \approx 3 \times 10^1$ cm $^{-3}$ at the expansion velocity of $v_{\text{exp}} \approx 28$ km s $^{-1}$. Possibly the wind-blown bubble of θ^2 Ori A has been disrupted by the stellar wind of θ^1 Ori C and merged with the second’s bubble.

4.6. The thermal bubbles of M 43 and NGC 1977

The ionizing stars of M 43 and NGC 1977 are of spectral types B0.5 and B1, respectively, and such stars have feeble stellar winds that are incapable of driving a bubble into their surroundings. We attribute the bubbles associated with these two nebulae to the thermal expansion of the ionized gas (Spitzer 1978). We will return to the stellar wind aspects later.

Simón-Díaz et al. (2011) conclude that M 43 is ionization-bounded. The Strömgren radius of the H II region envioning NU Ori with the rate of ionizing photons $\mathbb{N} \approx 1.5 \times 10^{47}$ s $^{-1}$ (Simón-Díaz et al. 2011) is $\mathcal{R}_S \approx 0.2$ pc (10^3 cm $^{-3}/n$) $^{2/3}$. Assuming the electron density Simón-Díaz et al. (2011) report, derived from optical line ratios, $n_e \approx 5 \times 10^2$ cm $^{-3}$, $\mathcal{R}_S \approx 0.3$ pc, which is in excellent agreement with the radius we measure.

After the initial phase of rapid ionization, the overpressure of the ionized gas compared to its environment drives the thermal expansion of the H II region (Krumholz & Matzner 2009; Spitzer 1978). For a homogeneous region, the present-time size and velocity of expansion (R_S , \dot{R}_S) are related to the expansion time and initial density (t_0 , n_0):

$$t_0 \approx 0.056 \left(\frac{R_S}{1 \text{ pc}} \right) \left(\frac{\dot{R}_S}{c_s} \right)^{4/3} \left(\left(\frac{c_s}{\dot{R}_S} \right)^{7/3} - 1 \right) \text{ Myr}, \quad (16)$$

$$n_0 \approx 56 \left(\frac{\mathbb{N}}{10^{47}} \right)^{1/2} \left(\frac{c_s}{\dot{R}_S} \right)^2 \left(\frac{1 \text{ pc}}{R_S} \right)^{3/2} \text{ cm}^{-3}, \quad (17)$$

where $c_s \approx 10$ km s $^{-1}$ is the sound speed in the ionized gas.

For M 43, we obtain with $R_S(t_0) \approx 0.3 \pm 0.05$ Myr and $v_{\text{exp}} = \dot{R}_S(t_0) \approx 6 \pm 2$ km s $^{-1}$ an expansion time of $t_0 \approx 0.02 \pm 0.01$ Myr and an initial density of $n_0 \approx 1.4 \pm 0.7 \times 10^3$ cm $^{-3}$. This implies that the star NU Ori is rather young. The expected main-sequence lifetime of a $\sim 20 M_\odot$ star like NU Ori is ~ 10 Myr.

From the H α emission in NGC 1977, we derive an electron density of $n_e \approx 35$ cm $^{-3}$ throughout the region, assuming a radius of $r \approx 1$ pc. With the rate of ionizing photons $\mathbb{N} \approx 1 \times 10^{45}$ s $^{-1}$ (Kim et al. 2016; Diaz-Miller et al. 1998), the Strömgren radius of the H II region surrounding 42 Orionis is $\mathcal{R}_S \approx 0.3$ pc. This is smaller than the size of the shell we observe. However, Hohle et al. (2010) give an effective temperature of $T_{\text{eff}} = 25$ 400 K for 42 Orionis. Also from its spectral class, B1V, we expect a much higher flux of ionizing photons, $\mathbb{N} \sim 1 \times 10^{47}$ s $^{-1}$ (Sternberg et al. 2003). We can estimate the rate of ionizing photons emitted by 42 Orionis (with minor assistance from other stars) from the H α emission in the H II region.

Table 8. Comparison of stellar parameters with bubble energetics of the three regions.

Region	Star	Stellar type	T_{eff} [K]	L_{\star} [L_{\odot}]	L_{w} [erg s $^{-1}$]	M_{shell} [M_{\odot}]	v_{exp} [km s $^{-1}$]	E_{kin} [erg]	t_0 [Myr]	$E_{\text{kin}}/(L_{\text{w}}t_0)$
M 42	θ^1 Ori C	O7V	3.9×10^4	2.0×10^5	8×10^{35}	1500	13	2.5×10^{48}	0.2	0.5
M 43	NU Ori	B0.5V	3.1×10^4	2.6×10^4	$\sim 3 \times 10^{31}$	7	6	3×10^{45}	0.02	50
NGC 1977	42 Ori	B1V	2.5×10^4	1.1×10^4	$\sim 3 \times 10^{31}$	700	1.5	2×10^{46}	0.4	40

Notes. In the last column, we take for t_0 the value derived from the stellar wind models; in case of M 43 the lifetime derived from pressure-driven expansion is a third of that value, increasing the ratio $E_{\text{kin}}/(L_{\text{w}}t_0)$ by a factor of three. Stellar parameters of θ^1 Ori C are from [Simón-Díaz et al. \(2006\)](#), of NU Ori from [Simón-Díaz et al. \(2011\)](#), and of 42 Orionis from [Hohle et al. \(2010\)](#).

Table 9. Masses, energetics, and luminosities in the expanding shells of M 42 (Veil shell), M 43, and NGC 1977.

	M 42 (Veil shell)	M 43	NGC 1977	References
$\dot{N}_{\text{Ly}\alpha}$ [10^{47} s $^{-1}$]	70	1.5	1	1, 2, 8
L_{w} [L_{\odot}]	400	$\sim 1.5 \times 10^{-2}$	$\sim 1.5 \times 10^{-2}$	3, 4
Mass of neutral gas [M_{\odot}]	1500	7	700	5, 8
Mass of ionized gas [M_{\odot}]	24	0.3	16	6, 8
E_{kin} of neutral gas [10^{46} erg]	250	0.3	2	5, 8
E_{kin} of ionized gas [10^{46} erg]	6	–	–	6, 7
E_{th} of ionized gas [10^{46} erg]	3	0.7	5	5, 8
E_{th} of hot gas [10^{46} erg]	10	–	–	3
L_{FIR} [L_{\odot}]	3.2×10^4	8.5×10^3	1.5×10^4	8
$L_{[\text{C III}]}$ [L_{\odot}]	170	24	140	8

Notes. There are no X-ray observations of the hot gas in M 43 and NGC 1977.

References. (1) [O’Dell et al. \(2017\)](#), (2) [Simón-Díaz et al. \(2011\)](#), (3) [Güdel et al. \(2008\)](#), (4) [Oskinova et al. \(2011\)](#), (5) [Pabst et al. \(2019\)](#), (6) [Wilson et al. \(1997\)](#), (7) [O’Dell \(2001\)](#), (8) this work.

We have:

$$L(\text{H}\alpha) = \int 4\pi j_{\text{H}\alpha} dV = \int \frac{4\pi j_{\text{H}\alpha}}{n_{\text{p}}n_{\text{e}}} n_{\text{p}}n_{\text{e}} dV, \quad (18)$$

$$\dot{N} = \int \alpha_{\text{B}} n_{\text{p}}n_{\text{e}} dV. \quad (19)$$

With $\frac{4\pi j_{\text{H}\alpha}}{n_{\text{p}}n_{\text{e}}} = 1.24 \times 10^{-25}$ erg cm 3 s $^{-1}$, $j_{\text{H}\alpha}/j_{\text{H}\beta} = 2.85$ ([Hummer & Storey 1987](#)), and $\alpha_{\text{B}} = 2.6 \times 10^{-13}$ cm 3 s $^{-1}$ ([Storey & Hummer 1995](#)) we obtain from the H α luminosity integrated over NGC 1977, $L(\text{H}\alpha) \simeq 45 L_{\odot}$, a photon rate of $\dot{N} \simeq 1 \times 10^{47}$ s $^{-1}$. With this value, we derive a present-day Strömgren radius of $R_{\text{S}} \simeq 1.5$ pc, which is in good agreement with the observed radius of the shell ($r = 1.0$ – 1.6 pc). With the extent of the expanding shell derived from the pv diagram in Fig. 17, $R_{\text{S}}(t_0) \simeq 1$ pc \pm 0.2, and the expansion velocity $v_{\text{exp}} = \dot{R}_{\text{S}}(t_0) \simeq 1.5 \pm 0.5$ km s $^{-1}$ the expansion time is $t_0 \simeq 0.4 \pm 0.2$ Myr and the initial density $n_0 \simeq 2.5 \pm 1.2 \times 10^3$ cm $^{-3}$. This, as well, suggests that 42 Orionis is rather young, compared to its expected lifetime of ~ 10 Myr.

4.7. Stellar wind versus thermal expansion of bubbles

In the previous sections, we analyze the kinematics of the bubbles around M 42, M 43, and NGC 1977 in terms of stellar-wind driven and thermal-pressure driven expansions, respectively. Here, we compare these two analyses. In Tables 8 and 9, we summarize our findings for the three regions.

For M 42, the momentum and energy in the ionized gas in the champagne-flow model is about two orders of magnitude

less than observed for the Veil shell: $22 M_{\odot}$ of ionized gas moving at 17 km s $^{-1}$ ([O’Dell 2001](#)) versus a (half)shell of $1500 M_{\odot}$ expanding at 13 km s $^{-1}$ (Table 9), the neutral Veil shell carrying a total momentum of $2 \times 10^4 M_{\odot}$ km s $^{-1}$. For M 43 and NGC 1977, on the other hand, the stellar wind is too feeble to drive the expansion of a large shell and the results are in good agreement with analytical models for the thermal expansion of H II regions. Figures 23 and 24 summarize this graphically. In this depiction, we have calculated the expected kinetic energy of a stellar wind bubble using the analytical model developed by [Weaver et al. \(1977\)](#),

$$E_{\text{kin}} \simeq \frac{6}{11} L_{\text{w}} t, \quad (20)$$

and the pressure-driven expansion of ionized gas ([Spitzer 1978](#)),

$$M_{\text{shell}} \simeq \frac{4\pi}{3} R_{\text{S},0}^3 \mu n_0 \left(1 + \frac{7t}{4t_{\text{s}}}\right)^{12/7}, \quad (21)$$

$$E_{\text{kin}} \simeq \frac{1}{2} M_{\text{shell}} c_{\text{s}}^2 \left(1 + \frac{7t}{4t_{\text{s}}}\right)^{-6/7}, \quad (22)$$

where $R_{\text{S},0} = \left(\frac{3\dot{N}}{4\pi n_0^2 \alpha_{\text{B}}}\right)^{1/3}$ is the initial Strömgren radius and $t_{\text{s}} = R_{\text{S},0}/c_{\text{s}}$. Comparing the predicted shell masses, where we assume that all the swept-up material is in the shell, to the measured masses as shown in Fig. 24, we observe that the measured masses of all three shells are slightly above the predictions, by a factor of about two. The mass discrepancy in M 42 and NGC 1977 might be due to our choice of β in the SEDs and a contamination from background material that is not expanding. The

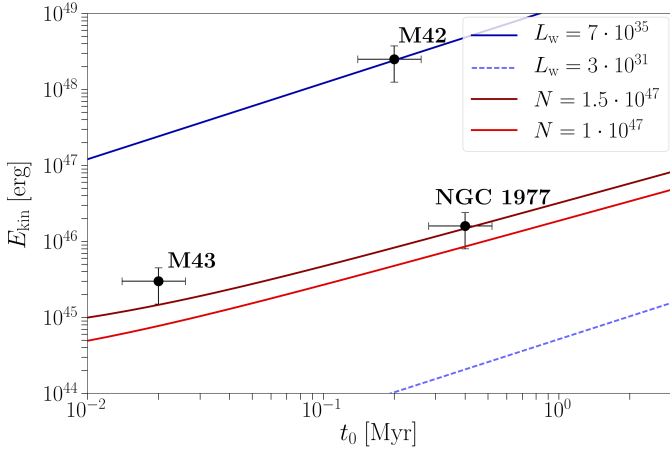


Fig. 23. Kinetic energy of expanding bubble shells versus expansion time. The lines are the predictions of wind models (blue) and models of pressure-driven expansion (red) with the parameters compiled in Tables 8 and 9.

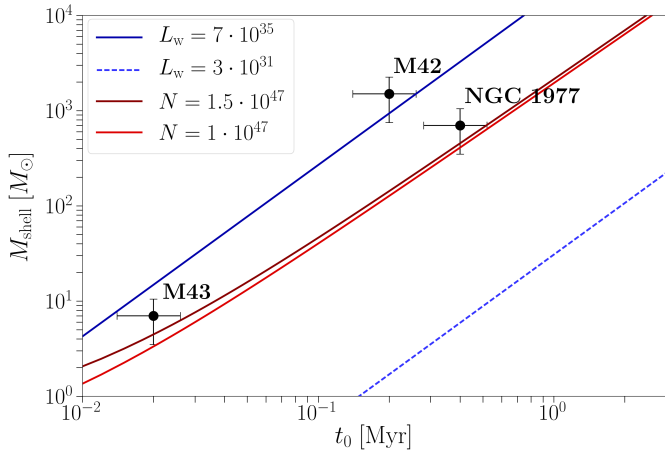


Fig. 24. Masses of expanding bubble shells versus expansion time. The lines are the predictions of wind models (blue) and models of pressure-driven expansion (red) with the parameters compiled in Tables 8 and 9.

mass of M43, estimated from the gas density in the shell, is a rather rough estimate as well.

For the Veil shell, the kinetic energy is comparable to the integrated wind luminosity of a wind-blown bubble. In M43 and NGC 1977, the observed kinetic energy of the shells much exceeds the integrated wind luminosity. For M43 and NGC 1977, the kinetics of the shell are in good agreement with the thermal expansion of the H II region, while for M42 this falls short by two orders of magnitude.

From models of O stars and comparison with real O stars (Pauldrach et al. 2001), we obtain an upper limit of $L_w \approx 1 \times 10^{34} \text{ erg s}^{-1}$. In their models of earlier B stars, however, even a B0.5V star has a significant stellar wind with $L_w \approx 1 \times 10^{33} \text{ erg s}^{-1}$ (Sternberg et al. 2003). Since no X-ray observations are available for M43 and NGC 1977, that might reveal gas shock-heated from stellar winds in the bubble interior as in M42, we cannot judge conclusively on this matter.

5. Conclusion

We have observed the [C II] emission from the Orion Nebula M42, M43, and NGC 1973, 1975, and 1977. Velocity-resolved

observations of the [C II] fine-structure line provide a unique tool to accurately quantify the kinematics of expanding bubbles in the ISM, in our case the large bubble associated with the Orion Nebula, the Orion Veil, and the bubbles of M43 and NGC 1973, 1975, and 1977. Our extended map of [C II] emission can be further used to disentangle dynamic structures within the same region on larger scales than previously possible. From the consistent arc structures in the pv diagrams and the line profiles, we are able to show that the gas is indeed expanding coherently on large scales as a bubble is blown into the ISM by stellar feedback.

We have compared three regions within the Orion Nebula complex that host different central stars causing the disruption of the molecular cloud cores in which these stars are born. The Orion Nebula M42 hosts the most massive star, an O-type star, which has a strong wind, that drives the expansion of the surrounding medium. M43 and NGC 1977 host less massive stars of early B type with much weaker winds. Still, both are effective in blowing bubbles of significant extent.

Pabst et al. (2019) have demonstrated that the Veil shell is a coherent, half-spherical structure, enclosing the layers of ionized gas observed towards that region. The stellar wind from θ^1 Ori C seems to be very effective in sweeping up its surrounding gas into a large-scale dense shell, leaving the bubble interior filled with dilute, hot X-ray emitting gas. This precise structure, a thin, rather cold shell of swept-up gas enveloping a hot interior medium, is characteristic of wind-blown bubbles. The bubble of the Orion Nebula, though still closed, may be on the brink of entering the bursting phase, thus rejuvenating the medium of the Orion-Eridanus superbubble.

The bubbles associated with M43 and NGC 1977 also exhibit spherical symmetry and possess a rather thin shell. In these two cases, however, the masses and kinetics of these shells are incompatible with an origin in a wind-driven shell. Instead, these shells are due to the pressure-driven expansion of the ionized gas and the observations are in good agreement with simple analytical estimates. All structures we have investigated here are rather young compared to the total lifetime of the driving (massive) stars. As stars in the Orion Nebula cluster will go off as supernovae, these structures will be disrupted as they age.

Acknowledgements. This work is based on observations made with the NASA/DLR Stratospheric Observatory for Infrared Astronomy (SOFIA). SOFIA is jointly operated by the Universities Space Research Association, Inc. (USRA), under NASA contract NNA17BF53C, and the Deutsches SOFIA Institut (DSI) under DLR contract 50 OK 0901 to the University of Stuttgart. J.R.G. thanks the ERC and the Spanish MCIU for funding support under grants ERC-2013-Syg-610256-NANOCOSMOS and AYA2017-85111-P, respectively. Research on the interstellar medium at Leiden Observatory is supported through a Spinoza award of the Dutch Science Organisation (NWO). We are grateful for the dedicated work during the upGREAT square-degree survey of Orion of the USRA and NASA staff of the Armstrong Flight Research Center in Palmdale and of the Ames Research Center in Mountain View, and the DSI. We thank C.R. O'Dell for commenting on an earlier version of the manuscript and helpful discussions. We thank the anonymous referee for comments that helped improve the manuscript.

References

- Abel, N. P., Ferland, G. J., O'Dell, C. R., & Troland, T. H. 2016, *ApJ*, **819**, 136
- Abel, N. P., Ferland, G. J., & O'Dell, C. R. 2019, *ApJ*, **881**, 130
- Allers, K. N., Jaffe, D. T., Lacy, J. H., Draine, B. T., & Richter, M. J. 2005, *ApJ*, **630**, 368
- Arthur, S. J. 2012, *MNRAS*, **421**, 1283
- Bedijn, P. J., & Tenorio-Tagle, G. 1981, *A&A*, **98**, 85
- Bernard-Salas, J., Habart, E., Arab, H., et al. 2012, *A&A*, **538**, A37
- Berné, O., & Matsumoto, Y. 2012, *ApJ*, **761**, L4
- Berné, O., Marcelino, N., & Cernicharo, J. 2010, *Nature*, **466**, 947
- Berné, O., Marcelino, N., & Cernicharo, N. 2014, *ApJ*, **795**, 13
- Bohlin, R. C., Savage, B. D., & Drake, J. F. 1978, *ApJ*, **224**, 132

- Boreiko, R. T., & Betz, A. L. 1996, *ApJ*, **467**, L113
- Bron, E., Agúndez, M., Goicoechea, J. R., & Cernicharo, J. 2018, *A&A*, submitted [arXiv:1801.01547]
- Carlyle, J., & Hillier, A. 2017, *A&A*, **605**, A101
- Castor, J., McCray, R., & Weaver, R. 1975, *ApJ*, **200**, L107
- Chevalier, R. A., Blondin, J. M., & Emmering, R. T. 1992, *ApJ*, **392**, 118
- Churchwell, E., Povich, M. S., Allen, D., et al. 2006, *ApJ*, **649**, 759
- Chuss, D. T., Andersson, B.-G., Bally, J., et al. 2019, *ApJ*, **872**, 187
- Cuadrado, S., Salas, P., Goicoechea, J. R., et al. 2019, *A&A*, **625**, L3
- Dale, J. E., Ngoumou, J., Ercolano, B., & Bonnell, I. 2013, *MNRAS*, **436**, 3430
- Da Rio, N., Robberto, M., Soderblom, D. R., et al. 2009, *ApJS*, **183**, 261
- Da Rio, N., Tan, J. C., & Jaehing, K. 2014, *ApJ*, **795**, 55
- Diaz-Miller, I. R., Franco, J., & Shore, S. N. 1998, *ApJ*, **501**, 192
- Duffell, P. C. 2016, *ApJ*, **821**, 76
- Freyer, T., Hensler, G., & Yorke, H. 2006, *ApJ*, **638**, 262
- García-Díaz, M. T., & Henney, W. J. 2007, *AJ*, **133**, 952
- García-Díaz, M. T., Henney, W. J., López, J. A., & Doi, T. 2008, *Rev. Mex. Astron. Astrofis.*, **44**, 181
- Goicoechea, J. R., Teyssier, D., Etxaluze, M., Goldsmith, P. F., & Ossenkopf, V. 2015, *ApJ*, **812**, 75
- Goicoechea, J. R., Pety, J., Cuadrado, S., et al. 2016, *Nature*, **537**, 207
- Goicoechea, J. R., Pabst, C. H. M., Kabanovic, S., et al. 2020, *A&A*, **639**, A1
- Goldsmith, P. F., Langer, W. D., Pineda, J. L., & Velusamy, T. 2012, *ApJS*, **203**, 13
- Griffin, M. J., Abergel, A., Abreu, A., et al. 2010, *A&A*, **518**, L3
- Großschedl, J. E., Alves, J., Meingast, S., et al. 2018, *A&A*, **619**, A106
- Großschedl, J. E., Alves, J., Teixeira, P. S., et al. 2019, *A&A*, **622**, A149
- Güdel, M., Briggs, K. R., Montmerle, T., et al. 2008, *Science*, **319**, 309
- Haid, S., Walch, S., Seifried, D., et al. 2018, *MNRAS*, **478**, 4799
- Hillenbrand, L. A. 1997, *ApJ*, **113**, 1733
- Hohle, M. M., Neuhauser, R., & Schutz, B. F. 2010, *Astron. Nachr.*, **331**, 349
- Hollenbach, D. J., & Tielens, A. G. G. M. 1999, *Rev. Mod. Phys.*, **71**, 1
- Hollenbach, D. J., Takahashi, T., & Tielens, A. G. G. M. 1991, *ApJ*, **377**, 192
- Hopkins, P. F., Quataert, E., & Murray, N. 2012, *MNRAS*, **421**, 3488
- Howarth, I. D., & Prinja, R. K. 1989, *ApJS*, **69**, 527
- Hummer, D. G., & Storey, P. J. 1987, *MNRAS*, **224**, 801
- Joblin, C., Bron, E., Pinto, C., et al. 2018, *A&A*, **615**, A129
- Kaufman, M. J., Wolfire, M. G., & Hollenbach, D. J. 2006, *ApJ*, **644**, 283
- Kim, J. S., Clarke, C. J., Fang, M., & Facchini, S. 2016, *ApJ*, **826**, L15
- Knyazeva, L. N., & Kharitonov, A. V. 1998, *Astron. Rep.*, **42**, 60
- Kounkel, M., Hartmann, L., Loinard, L., et al. 2017, *ApJ*, **834**, 142
- Kraus, S., Weigelt, G., Balega, Y. Y., et al. 2009, *A&A*, **497**, 195
- Krumholz, M. R., & Matzner, C. D. 2009, *ApJ*, **703**, 1352
- Langer, W. D., & Penzias, A. A. 1990, *ApJ*, **357**, 477
- Lehmann, H., Vitrichenko, E., Bychkov, V., Bychkova, L., & Klochkova, V. 2010, *A&A*, **514**, A34
- Li, A., & Draine, B. T. 2001, *ApJ*, **544**, 778
- Lombardi, M., Bouy, H., Alves, J., & Lada, C. J. 2014, *A&A*, **566**, A45
- Mac Low, M.-M., & McCray, R. 1988, *ApJ*, **324**, 776
- Marconi, A., Testi, L., Natta, A., & Walmsley, C. M. 1998, *A&A*, **330**, 696
- McCray, R., & Kafatos, M. 1987, *ApJ*, **317**, 190
- McKee, C. F., & Ostriker, J. P. 1977, *ApJ*, **218**, 148
- Megeath, S. T., Gutermuth, R., Muzerolle, J., et al. 2012, *AJ*, **144**, 192
- Megeath, S. T., Gutermuth, R., Muzerolle, J., et al. 2016, *AJ*, **151**, 5
- Megier, A., Strobel, A., Bondar, A., et al. 2005, *ApJ*, **634**, 451
- Menten, K. M., Reid, M. J., Forbrich, J., & Brunthaler, A. 2007, *A&A*, **474**, 515
- Nakamura, F., McKee, C. F., Klein, R. I., & Fisher, R. T. 2006, *ApJS*, **164**, 477
- Norman, C. A., & Ikeuchi, S. 1989, *ApJ*, **345**, 372
- Ochsendorf, B. B., Verdolini, S., Cox, N. L. J., et al. 2014, *A&A*, **566**, A75
- Ochsendorf, B. B., Brown, A. G. A., Bally, J., & Tielens, A. G. G. M. 2015, *ApJ*, **808**, 111
- O'Dell, C. R. 2001, *ARA&A*, **39**, 99
- O'Dell, C. R. 2018, *MNRAS*, **478**, 1017
- O'Dell, C. R., & Goss, W. M. 2009, *AJ*, **138**, 1235
- O'Dell, C. R., & Harris, J. A. 2010, *ApJ*, **140**, 985
- O'Dell, C. R., & Yusef-Zadeh, F. 2000, *ApJ*, **120**, 382
- O'Dell, C. R., Henney, W. J., Abel, N. P., Ferland, G. J., & Arthur, S. J. 2009, *ApJ*, **137**, 367
- O'Dell, C. R., Kollatschny, W., & Ferland, G. J. 2017, *ApJ*, **837**, 151
- Oskinova, L. M., Todt, H., Ignace, R., et al. 2011, *MNRAS*, **416**, 1456
- Ossenkopf, V., Röllig, M., Neufeld, D. A., et al. 2013, *A&A*, **550**, A57
- Ostriker, J. P., & McKee, C. F. 1988, *Rev. Mod. Phys.*, **60**, 1
- Pabst, C. H. M., Goicoechea, J. R., Teyssier, D., et al. 2017, *A&A*, **606**, A29
- Pabst, C., Higgins, R., Goicoechea, J. R., et al. 2019, *Nature*, **565**, 618
- Pauldrach, A. W. A., Hoffmann, T. L., & Lennon, M. 2001, *A&A*, **375**, 161
- Pellegrini, E. W., Baldwin, J. A., Ferland, G. J., Shaw, G., & Heathcote, S. 2009, *ApJ*, **693**, 285
- Peterson, D. E., & Megeath, S. T. 2008, *Handbook of Star Forming Regions* (San Francisco, USA: Astronomical Society of the Pacific), 1
- Petit, V., Owocki, S. P., Oksala, M. E., & the MiMeS Collaboration 2012, *ASP Conf. Ser.*, **465**, 48
- Poglitsch, A., Waelkens, C., Geis, N., et al. 2010, *A&A*, **518**, L2
- Pound, M. W., & Wolfire, M. G. 2008, *ASP Conf. Ser.*, **394**, 654
- Prosser, C. F., Stauffer, J. R., Hartmann, L., et al. 1994, *ApJ*, **421**, 517
- Risacher, C., Güsten, R., Stutzki, J., et al. 2016, *A&A*, **595**, A34
- Salgado, F., Berné, O., Adams, J. D., et al. 2016, *ApJ*, **830**, 118
- Schulz, N. S., Testa, P., Huenemoerder, D. P., Ishibashi, K., & Canizares, C. 2006, *ApJ*, **653**, 636
- Silich, S., & Tenorio-Tagle, G. 2013, *ApJ*, **765**, 43
- Simón-Díaz, S., Herrero, A., Esteban, C., & Najarro, F. 2006, *A&A*, **448**, 351
- Simón-Díaz, S., García-Rojas, J., Esteban, C., et al. 2011, *A&A*, **530**, A57
- Sofia, U. J., Lauroesch, J. T., Meyer, D. M., & Cartledge, S. I. B. 2004, *ApJ*, **605**, 272
- Spitzer, L. 1978, *Physical Processes in the Interstellar Medium* (New York: Wiley-Interscience)
- Stahl, O., Kaufer, A., Rivinius, T., et al. 1996, *A&A*, **312**, 539
- Stahl, O., Wade, G., Petit, V., Stober, B., & Schanne, L. 2008, *A&A*, **487**, 323
- Sternberg, A., Hoffmann, T. L., & Pauldrach, A. W. A. 2003, *ApJ*, **599**, 1333
- Stone, J. M., & Gardiner, T. 2007, *ApJ*, **671**, 1726
- Storey, P. J., & Hummer, D. G. 1995, *MNRAS*, **272**, 41
- Störzer, H., & Hollenbach, D. 1999, *ApJ*, **515**, 669
- Subrahmanyan, R., Goss, W. M., & Malin, D. F. 2001, *AJ*, **121**, 399
- Tielens, A. G. G. M. 2010, *The Physics and Chemistry of the Interstellar Medium* (New York: Cambridge University Press)
- Tielens, A. G. G. M., Meixner, M. M., van der Werf, P. P., et al. 1993, *Science*, **262**, 86
- Troland, T. H., Goss, W. M., Brogan, C. L., Crutcher, R. M., & Roberts, D. A. 2016, *ApJ*, **825**, 2
- Van der Werf, P. P., Goss, W. M., & O'Dell, C. R. 2013, *ApJ*, **762**, 101
- Vitrichenko, E. A. 2002, *Astron. Lett.*, **28**, 324
- Walch, S. K., Whitworth, A. P., Bisbas, T., Wunsch, R., & Hubber, D. 2012, *MNRAS*, **427**, 625
- Walch, S., Whitworth, A. P., Bisbas, T. G., Wunsch, R., & Hubber, D. 2013, *MNRAS*, **435**, 917
- Wareing, C. J., Pittard, J. M., Wright, N. J., & Falle, S. A. E. G. 2018, *MNRAS*, **475**, 3598
- Weaver, R., McCray, R., Castor, J., Shapiro, P., & Moore, R. 1977, *ApJ*, **218**, 377
- Weilbacher, P. M., Monreal-Ibero, A., Kollatschny, W., et al. 2015, *A&A*, **582**, A114
- Weingartner, J. C., & Draine, B. T. 2001, *ApJ*, **548**, 296
- Williams, J. P., & McKee, C. F. 1997, *ApJ*, **476**, 166
- Wilson, T. L., Filges, L., Codella, C., Reich, W., & Reich, P. 1997, *A&A*, **327**, 1177

Appendix A: SED results

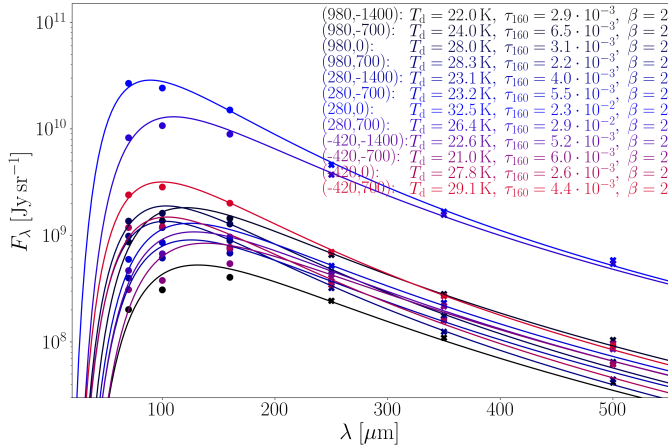


Fig. A.1. SED fits to individual points throughout the Orion Nebula complex. The flux in the PACS bands is plotted as circles; fluxes of the SPIRE bands are plotted as crosses. Numbers in brackets are the RA and Dec offset, respectively, in arc seconds.

Figure A.1 shows the results from an SED fit in individual points with the emissivity index $\beta = 2$. The derived dust temperature decreases with increasing β , while the dust optical depth increases significantly. The integrated FIR intensity does not depend strongly on β .

Appendix B: The expanding Rim

We present here our analysis of the kinematics in the eastern bright arm, the so-called Eastern Rim, of the expanding shell. To estimate the three-dimensional expansion velocity, we make use of the following formula:

$$v_{\text{exp}} = \frac{v_2 - v_1}{\sqrt{1 - \frac{r_1^2}{r_2^2}}}, \quad (\text{B.1})$$

where $v_2 - v_1$ is the velocity difference of the velocity channels considered; r_1 and r_2 are the respective distances of the emission filament in these two channels. r_2 is the further outward lying filament, for an accurate calculation it must be the outermost. We can write $r_1 = r_2 - \Delta r$, where Δr is the separation between the two channel filaments. If $v_2 > v_1$, the shell is moving toward us and we assign a positive expansion velocity; else it is expanding away from us. Here, we use the [C II] channels at $v_{\text{LSR}} = 0-1 \text{ km s}^{-1}$, $v_{\text{LSR}} = 2-3 \text{ km s}^{-1}$ and $v_{\text{LSR}} = 4-5 \text{ km s}^{-1}$. With $v_2 - v_1 = 2 \text{ km s}^{-1}$, $r_2 \approx 1.75 \text{ pc}$ and $\Delta r \approx 0.2 \text{ pc}$ (cf Fig. B.1), we obtain $v_{\text{exp}} \approx 4.25 \text{ km s}^{-1}$. We note that only the distance of the furthest filament (cf. Fig. B.2) gives an accurate measure of the extent of the expanding shell, which renders the estimate from the three channels used here somewhat inaccurate; however, in higher-velocity channels the displacement between the filamentary structures is not as clear-cut as it is in these channels.

We detect the $^{13}\text{C II}$ $F = 2-1$ line in averaged spectra in this region as shown in Fig. B.3. From the peak temperatures of the $^{12}\text{C II}$ and $^{13}\text{C II}$ line (Table B.1), we compute the [C II] optical depth by Eqs. (3) and (4). The C^+ column density is given by Eq. (6). The analysis yields $\tau_{[\text{C II}]} \approx 3$. From the column density, we estimate a gas density of the limb-brightened shell from $n = N_{\text{C}^+} / ([\text{C}/\text{H}]l)$, where $[\text{C}/\text{H}] \approx 1.6 \times 10^{-4}$ (Sofia et al. 2004)

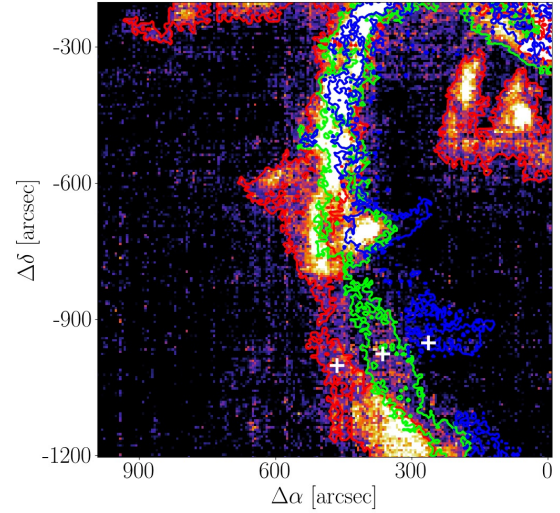


Fig. B.1. Color map of [C II] emission in velocity interval $v_{\text{LSR}} = 0-5 \text{ km s}^{-1}$, with contours of the channel emission in $v_{\text{LSR}} = 0-1 \text{ km s}^{-1}$, $v_{\text{LSR}} = 2-3 \text{ km s}^{-1}$, and $v_{\text{LSR}} = 4-5 \text{ km s}^{-1}$ (blue, green, and red, respectively). From the displacement of the structure of brightest emission in these channels with respect to each other, points marked by the white crosses, we can estimate the expansion velocity to be $v_{\text{exp}} \approx 4.25 \text{ km s}^{-1}$. The projected distance between the crosses is 0.2 pc , and the projected distance from the Trapezium stars of the outermost filament, traced by blue contours, is 1.75 pc .

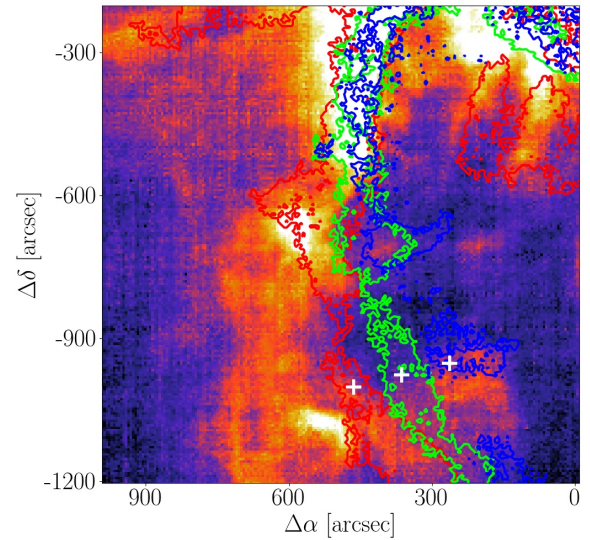


Fig. B.2. Color map of [C II] emission in velocity interval $v_{\text{LSR}} = 0-15 \text{ km s}^{-1}$, with contours of the channel emission in $v_{\text{LSR}} = 0-1 \text{ km s}^{-1}$, $v_{\text{LSR}} = 2-3 \text{ km s}^{-1}$, and $v_{\text{LSR}} = 4-5 \text{ km s}^{-1}$ (blue, green, and red, respectively). The expanding filament grows brighter as it moves outward, probably mainly due to increasing limb-brightening, so the color map is dominated by the most outward filament.

and the extent l along the line of sight is $l \approx r/2 \approx 1 \text{ pc}$. This yields $n \approx 1 \times 10^4 \text{ cm}^{-3}$.

Figure B.4 compares the CO(2-1) emission with the [C II] emission in the expanding Rim, that is observed in the velocity range $v_{\text{LSR}} = 5-8 \text{ km s}^{-1}$. From the peak separation in line cut 1, $d \approx 70'' \approx 0.14 \text{ pc}$, we derive a density of $n \approx 9 \times 10^3 \text{ cm}^{-3}$ in the Rim. From line cut 2 ($d \approx 110'' \approx 0.22 \text{ pc}$), we derive a density of $n \approx 6 \times 10^3 \text{ cm}^{-3}$ in the south of the bright Rim.

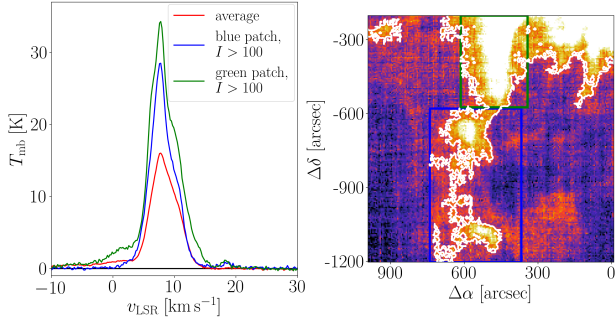


Fig. B.3. *Right:* [C II] line-integrated intensity in the bright eastern Rim. White contours indicate $I_{[\text{C II}]} > 100 \text{ K km s}^{-1}$. *Left:* averaged spectra from this region as indicated. Results of the analysis of the peak temperatures are given in Table B.1.

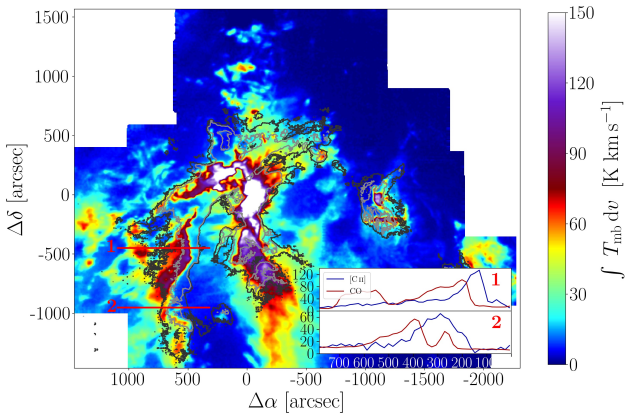


Fig. B.4. $^{12}\text{CO}(2-1)$ emission in velocity interval $v_{\text{LSR}} = 5-8 \text{ km s}^{-1}$ with [C II] emission in same velocity interval in contours (dark grey: 30 K km s^{-1} , light grey: 50 K km s^{-1}). The inlaid panels show the line cuts along the two red lines indicated in the figure.

From the dust optical depth, we estimate a mean $\tau_{160} \simeq 4 \times 10^{-3}$ in the [C II]-bright regions. This translates to a gas

Table B.1. Gaussian fit parameters of spectra in Fig. B.3.

	$T_{\text{P}}(^{12}\text{C II})$ [K]	$T_{\text{P}}(^{13}\text{C II})$ [K]	$\tau_{[\text{C II}]}$	T_{ex} [K]	N_{C^+} [cm^{-2}]
Green	35	1	2.9	48	5.7×10^{18}
Blue	30	1	3.4	44	6.4×10^{18}

column density of $N_{\text{H}} \simeq 2 \times 10^{22} \text{ cm}^{-2}$. Assuming that all carbon is ionized, this results in a C^+ column density of $N_{\text{C}^+} \simeq 3 \times 10^{18} \text{ cm}^{-2}$, which is a factor of 2 lower than what we estimate from the [C II] spectra. Since τ_{160} strongly depends on the choice of the grain emissivity index β , the agreement might be satisfactory. However, it might be a hint that we overestimate the [C II] optical depth and underestimate the excitation temperature. With these given the physical temperature of the gas would be $T \simeq 50 \text{ K}$, which is lower than expected from the PDR models for the [C II]-emitting (surface) layers. At these high opacities opacity broadening of the line might also become significant, which is not what we observe. The fitting procedure is complicated by the presence of multiple components. The main line can be fitted by two emission components or by one emission and one absorption component. However, the latter would increase the result for $\tau_{[\text{C II}]}$ even further. In conclusion, the values obtained here can only be a crude estimate due to the complex emission structure from this region, which might be inadmissibly averaged together in the spectra.

Appendix C: PV diagrams

Figures C.1–C.4 show the pv diagrams resulting from slicing the velocity-resolved [C II] map from the Extended Orion Nebula with M43 and NGC 1977 along the RA and Dec axis, respectively. The coherent arc structure indicative of the expansion of the Veil shell can be seen in almost all pv diagrams. The expanding structure of NGC 1977 is more difficult to recognize.

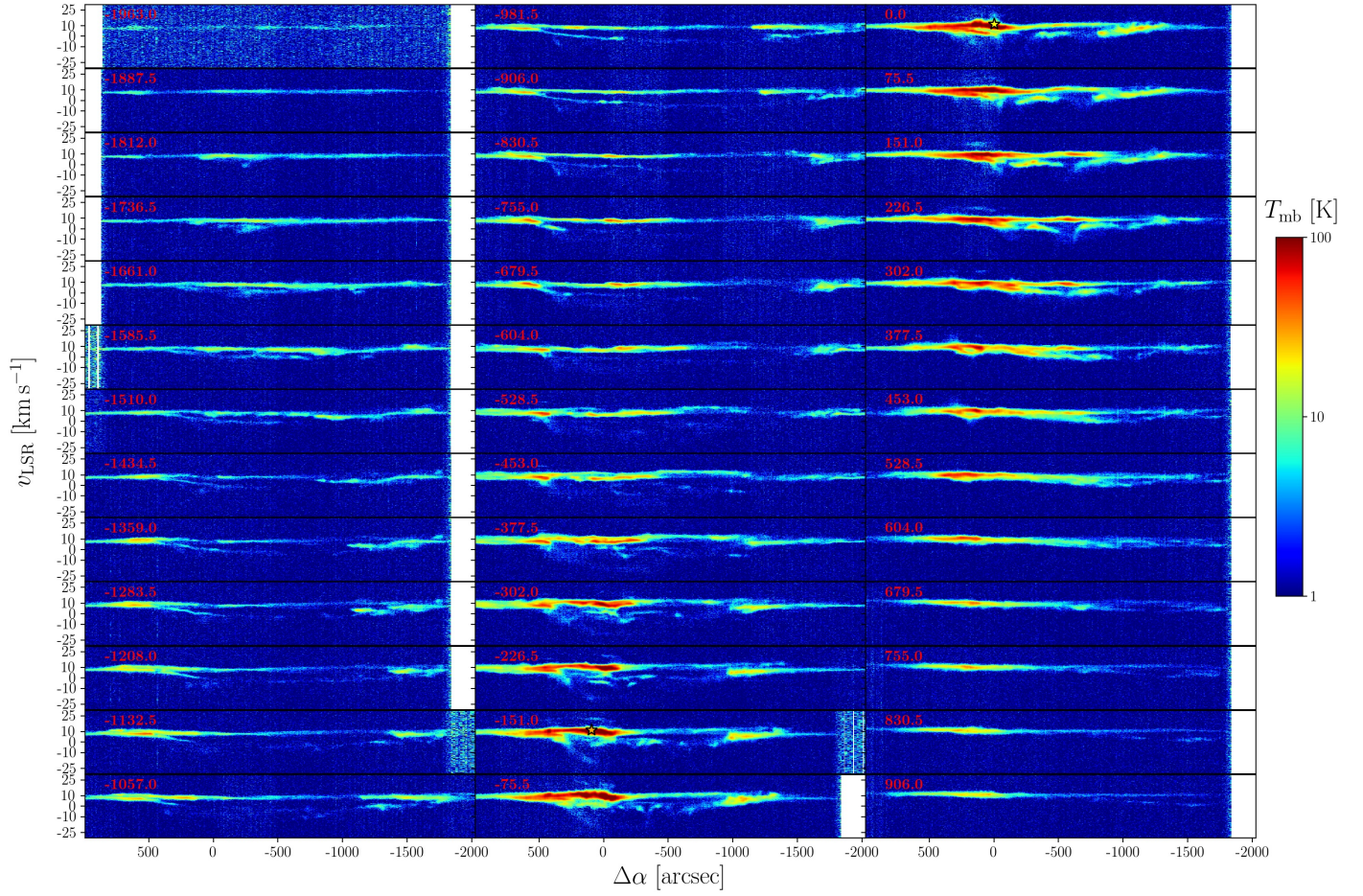


Fig. C.1. [C II] pv diagrams from the Veil shell, sliced along RA axis. Red numbers are the respective Dec offsets in arc seconds.

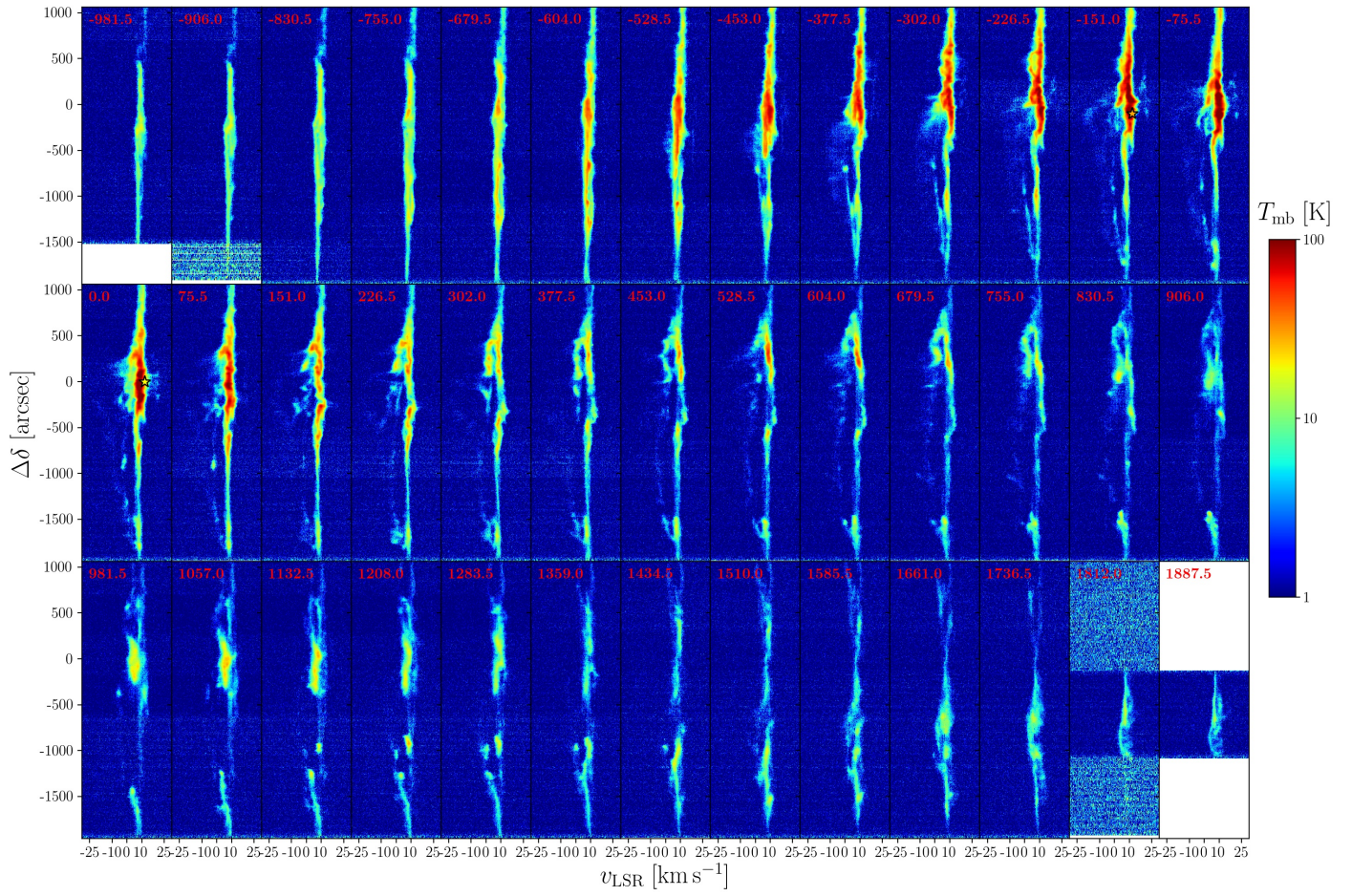


Fig. C.2. [C II] pv diagrams from the Veil shell, sliced along Dec axis. Red numbers are the respective RA offsets in arc seconds.

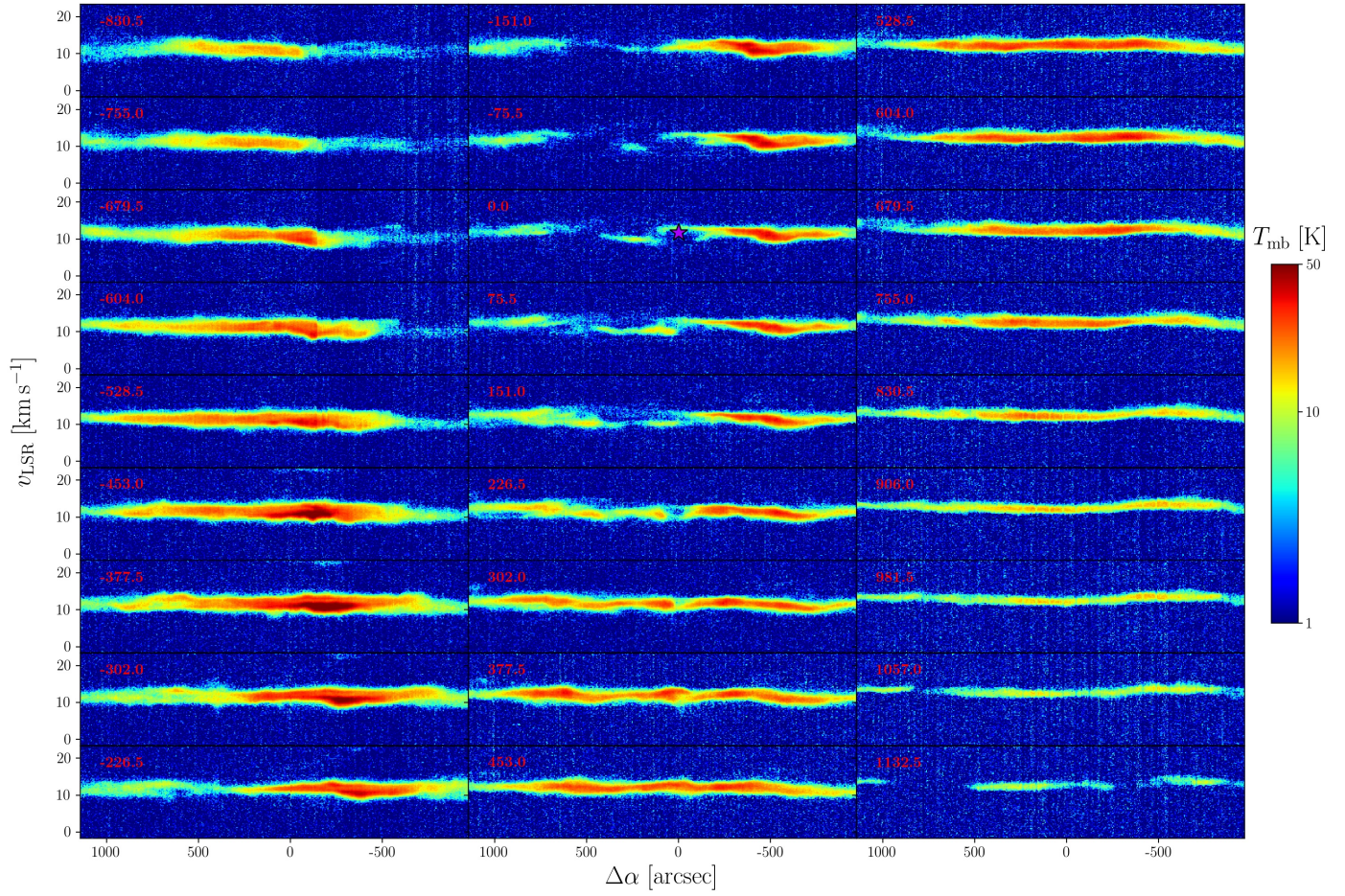


Fig. C.3. [C II] pv diagrams from NGC 1977, sliced along RA axis. Red numbers are the respective Dec offsets in arc seconds. Coordinate offsets are given with respect to the position of 42 Orionis.

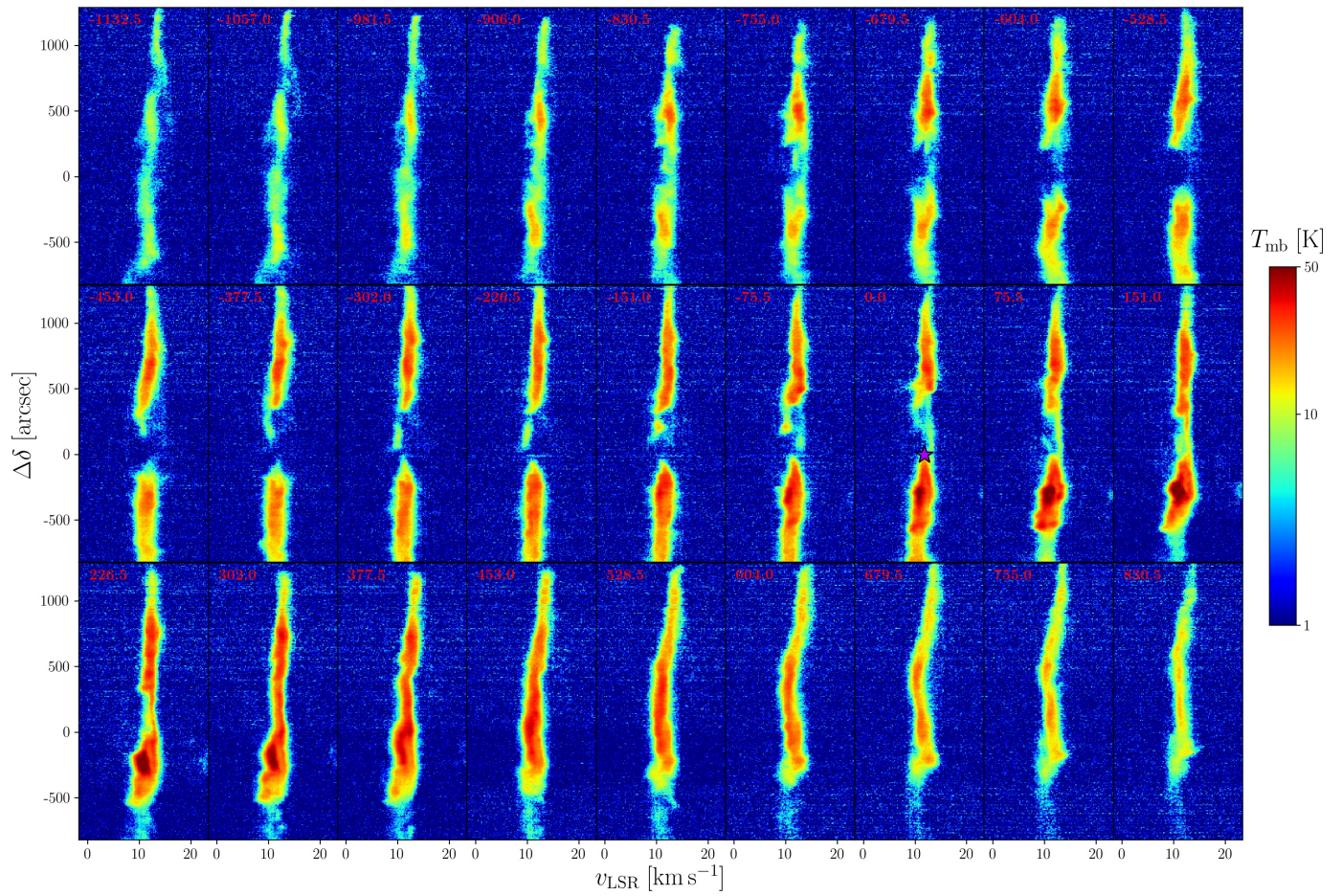


Fig. C.4. [C II] pv diagrams from NGC 1977, sliced along Dec axis. Red numbers are the respective RA offsets in arc seconds. Coordinate offsets are given with respect to the position of 42 Orionis.